The Astronomical Journal, 160:181 (29pp), 2020 October https://doi.org/10.3847/1538-3881/abacb6

The Southern Stellar Stream Spectroscopic Survey (S^5): Chemical Abundances of Seven Stellar Streams

Alexander P. Ji[1,22], Ting S. Li[1,2,23], Terese T. Hansen[3,4], Andrew R. Casey[5], Sergey E. Koposov[6,7,8,9], Andrew B. Pace[6], Dougal Mackey[10], Geraint F. Lewis[11], Jeffrey D. Simpson[12,13], Joss Bland-Hawthorn[11,13], Lara R. Cullinane[10], Gary. S. Da Costa[10], Kohei Hattori[6], Sarah L. Martell[12,13], Kyler Kuehn[14,15], Denis Erkal[16], Nora Shipp[17,18,19], Zhen Wan[11], and Daniel B. Zucker[20,21]

[1] Observatories of the Carnegie Institution for Science, 813 Santa Barbara St., Pasadena, CA 91101, USA; aji@carnegiescience.edu
[2] Department of Astrophysical Sciences, Princeton University, Princeton, NJ 08544, USA
[3] George P. and Cynthia Woods Mitchell Institute for Fundamental Physics and Astronomy, and Department of Physics and Astronomy, Texas A&M University, College Station, TX 77843, USA
[4] Department of Physics and Astronomy, Texas A&M University, College Station, TX 77843, USA
[5] School of Physics and Astronomy, Monash University, Wellington Rd., Clayton, VIC 3800, Australia
[6] McWilliams Center for Cosmology, Carnegie Mellon University, 5000 Forbes Ave., Pittsburgh, PA 15213, USA
[7] Institute for Astronomy, University of Edinburgh, Royal Observatory, Blackford Hill, Edinburgh EH9 3HJ, UK
[8] Institute of Astronomy, University of Cambridge, Madingley Rd., Cambridge CB3 0HA, UK
[9] Kavli Institute for Cosmology, University of Cambridge, Madingley Rd., Cambridge CB3 0HA, UK
[10] Research School of Astronomy and Astrophysics, Australian National University, Canberra, ACT 2611, Australia
[11] Sydney Institute for Astronomy, School of Physics, A28, The University of Sydney, NSW 2006, Australia
[12] School of Physics, UNSW, Sydney, NSW 2052, Australia
[13] Centre of Excellence for All-Sky Astrophysics in Three Dimensions (ASTRO 3D), Australia
[14] Lowell Observatory, 1400 W. Mars Hill Rd., Flagstaff, AZ 86001, USA
[15] Australian Astronomical Optics, Faculty of Science and Engineering, Macquarie University, Macquarie Park, NSW 2113, Australia
[16] Department of Physics, University of Surrey, Guildford GU2 7XH, UK
[17] Department of Astronomy & Astrophysics, University of Chicago, 5640 S. Ellis Ave., Chicago, IL 60637, USA
[18] Kavli Institute for Cosmological Physics, University of Chicago, Chicago, IL 60637, USA
[19] Fermi National Accelerator Laboratory, P.O. Box 500, Batavia, IL 60510, USA
[20] Department of Physics & Astronomy, Macquarie University, Sydney, NSW 2109, Australia
[21] Macquarie University Research Centre for Astronomy, Astrophysics & Astrophotonics, Sydney, NSW 2109, Australia
Received 2020 May 27; revised 2020 August 3; accepted 2020 August 4; published 2020 September 24

Abstract

We present high-resolution Magellan/MIKE spectroscopy of 42 red giant stars in seven stellar streams confirmed by the Southern Stellar Stream Spectroscopic Survey (S^5): ATLAS, Aliqa Uma, Chenab, Elqui, Indus, Jhelum, and Phoenix. Abundances of 30 elements have been derived from over 10,000 individual line measurements or upper limits using photometric stellar parameters and a standard LTE analysis. This is currently the most extensive set of element abundances for stars in stellar streams. Three streams (ATLAS, Aliqa Uma, and Phoenix) are disrupted metal-poor globular clusters, although only weak evidence is seen for the light-element anticorrelations commonly observed in globular clusters. Four streams (Chenab, Elqui, Indus, and Jhelum) are disrupted dwarf galaxies, and their stars display abundance signatures that suggest progenitors with stellar masses ranging from 10^6 to 10^7 $M_\odot$. Extensive description is provided for the analysis methods, including the derivation of a new method for including the effect of stellar parameter correlations on each star's abundance and uncertainty. This paper includes data gathered with the 6.5 m Magellan Telescopes located at Las Campanas Observatory, Chile.

Unified Astronomy Thesaurus concepts: Globular star clusters (656); Stellar abundances (1577); Dwarf galaxies (416); Milky Way stellar halo (1060)

Supporting material: machine-readable tables

1. Introduction

The Milky Way's stellar halo is a galactic graveyard that contains a record of past accretion events (e.g., Freeman & Bland-Hawthorn 2002; Johnston et al. 2008; Helmi 2020). Dwarf galaxies and globular clusters (GCs) fall into the Milky Way, become tidally unbound, and eventually mix into a smooth stellar halo. Stellar streams are the intermediate stage, when an object is in the midst of tidal disruption, but its stars are still spatially and kinematically coherent. Hundreds of streams from dozens of accreting objects are expected in the solar neighborhood (Helmi et al. 1999; Gómez et al. 2013). Indeed, the number of known stellar streams has exploded in recent years (e.g., Grillmair & Carlberg 2016; Mateu et al. 2018; Shipp et al. 2018; Ibata et al. 2019), in large part thanks to large photometric surveys like the Sloan Digital Sky Survey (SDSS; York et al. 2000; Stoughton et al. 2002) Dark Energy Survey (DES; DES Collaboration et al. 2018) and, more recently, all-sky proper motions from Gaia (Gaia Collaboration et al. 2016, 2018).

The detailed chemical abundances of stream stars are preserved even after the progenitor galaxy or cluster is disrupted. Chemodynamic studies of stellar streams are thus a powerful way to investigate the nature of the progenitor systems and directly see the buildup of the stellar halo through tidal disruption. Abundances can be used to determine whether a stream's progenitor is a dwarf galaxy or a globular cluster (e.g., Gratton et al. 2004; Tolstoy et al. 2009; Leaman 2012;

[22] Hubble Fellow.
[23] NHFP Einstein Fellow.

Willman & Strader 2012; Casey et al. 2014; Fu et al. 2018). They can also be used to confirm or reject an association between spatially separated stellar structures (e.g., Freeman & Bland-Hawthorn 2002; Bergemann et al. 2018; Kos et al. 2018; Marshall et al. 2019). Furthermore, tidally disrupting GCs and dwarf galaxies may probe different parts of parameter space compared to their intact counterparts. For example, metal-poor GCs might be more likely to be found as disrupted streams (e.g., Kruijssen 2019), while tidally disrupted dwarf galaxies may have had different accretion times or orbital histories compared to intact galaxies (e.g., Rocha et al. 2012).

Although more than 60 streams have been discovered, only a few have actually been chemically characterized. The Sagittarius stream is one of the most prominent structures in the sky and thus has been the subject of many abundance studies (e.g., Monaco et al. 2007; Chou et al. 2010; Keller et al. 2010; Battaglia et al. 2017; Carlin et al. 2018; Hayes et al. 2020). However, thus far, only seven other streams have been the subject of high-resolution spectroscopic abundance studies. Casey et al. (2014) studied three stars in the Orphan stream, showing that its progenitor was a dwarf galaxy; Frebel et al. (2013b) and Fu et al. (2018) studied a total of seven stars in the 300S stream, also finding that its progenitor was a dwarf galaxy; Jahandar et al. (2017) used APOGEE to study one likely stream member around the Palomar 1 globular cluster; Marshall et al. (2019) examined two stars in the stream around the actively disrupting ultra-faint dwarf galaxy Tucana III, confirming similar abundances in the stream and the galaxy core; Roederer & Gnedin (2019) studied two stars in the Sylgr stream, finding that its progenitor was likely an extremely metal-poor globular cluster; Simpson et al. (2020) tagged five members of the Fimbulthul stream to the globular cluster ω Cen; and Roederer et al. (2010) examined 12 stars in the Helmi et al. (1999) debris streams, finding that these stars chemically resemble the bulk of the Milky Way's stellar halo. With only 32 individual stars across seven streams, abundances in stellar streams are still rather sparse. Eventually, streams become so spatially incoherent that they are considered to be part of the general stellar halo, although the halo can still be broken into discrete components, like the Gaia–Enceladus–Sausage (e.g., Belokurov et al. 2018; Helmi et al. 2018) and myriad other chemodynamic groups (e.g., Kruijssen et al. 2019; Matsuno et al. 2019; Myeong et al. 2019; Mackereth & Bovy 2020; Naidu et al. 2020; Yuan et al. 2020).

The Southern Stellar Stream Spectroscopic Survey (S^5) has been using the 2-degree-field fiber positioner and AAOmega spectrograph (Lewis et al. 2002; Sharp et al. 2006) at the Anglo-Australian Telescope (AAT), along with proper motions from Gaia (Gaia Collaboration et al. 2016, 2018), to characterize the kinematics and metallicities of stars in stellar streams (Li et al. 2019; Shipp et al. 2019). So far, S^5 has characterized 12 streams with the AAT, and in this work, we focus on seven of the nine streams in the DES footprint (Shipp et al. 2018; Li et al. 2019). The ATLAS stream was initially discovered in the ATLAS survey (Koposov et al. 2014), and the Phoenix stream was found in the Phoenix constellation with the first year of DES data (Balbinot et al. 2016). The other five streams (Aliqa Uma, Chenab, Elqui, Indus, and Jhelum) were discovered using the first 3 yr of DES data and named after aquatic terms from different cultures (Shipp et al. 2018). All seven streams show clear tracks in position and velocity space that can be identified by eye (Li et al. 2019; Shipp et al. 2019). Serendipitously, S^5 has also discovered a star with an extreme velocity (Koposov et al. 2020).

This paper presents the results from high-resolution Magellan/MIKE (Bernstein et al. 2003) spectroscopic observations of 42 red giant stars selected from seven streams observed in the S^5 survey, including radial velocities and abundances for up to 35 species of 30 elements. We have observed five stars in Aliqa Uma, seven stars in ATLAS, three stars in Chenab, four stars in Elqui, seven stars in Indus, eight stars in Jhelum, and eight stars in Phoenix. Our results represent the most complete characterization of stellar stream abundances to date, doubling the total number of chemically characterized streams and the number of stars in those streams (excluding Sgr). In this paper, we focus on a detailed description of our abundance analysis methodology. Science results will be presented in other papers (A. R. Casey et al. 2020, in preparation; T. T. Hansen et al. 2020, in preparation; Li et al. 2020; A. Pace et al. 2020, in preparation). Section 2 presents the observation details and radial velocity measurements. Sections 3 and 4 present the stellar parameters and abundance analysis methods, with the resulting abundances presented in Section 5 and detailed comments on each element in Section 6. Brief comments on the character of each individual stream are given in Section 7 before concluding in Section 8. Appendix A compares the stellar parameters to other means of obtaining the parameters. Appendix B gives a pedagogical description of calculating abundance uncertainties. Appendix C shows the internal validation of the equivalent width and abundances. Appendix D gives several figures showing abundance correlations with stellar parameters.

2. Observations and Radial Velocities

The high-resolution targets were selected as the brightest ($r \lesssim 17.5$) member stars in these seven streams based on the kinematic and metallicity information from medium-resolution S^5 spectroscopy from the AAT (Lewis et al. 2002; Sharp et al. 2006). For the ATLAS, Aliqa Uma, and Phoenix streams (globular cluster origins, thin and cold), member stars were selected with a simple cut in proper motion and radial velocity (Li et al. 2020; Wan et al. 2020). For the other four dwarf galaxy origin streams, since the stream has a much larger velocity dispersion and their phase space information is more blended with the Milky Way foreground, a selection based on membership probability is used (A. Pace et al. 2020, in preparation). The membership probability of each star is calculated with a mixture model based on the spatial location of the star relative to the stream track, proper motion, radial velocity, and metallicity. High membership probability ($P > 0.7$) targets were selected for observation. Note that due to the limited telescope time, not all bright members were observed, and stars with the highest membership probability tend to be mostly metal-poor stars, especially for dwarf galaxy streams where the metallicity spread is large. Therefore, the sample presented here might not be representative of the metallicity distribution for these dwarf galaxy streams. We defer this discussion to the medium-resolution data in other S^5 publications, which contain a much larger sample of stream members with stellar metallicities.

These stars were observed with the Magellan/MIKE spectrograph (Bernstein et al. 2003) over four separate runs in 2018–2019, though most stars were observed in 2018 November and 2019 July (Table 1). The CCDs were binned 2×2, and slit widths of $0\farcs7$ and $1\farcs0$ were used depending on the seeing, resulting in typical resolutions of $R \sim 35k/28k$ and $28k/22k$ on the blue/red arms of

Table 1
Observations

Name	Source_ID	R.A. (h:m:s)	Decl. (d:m:s)	Obs. Date	MJD	g (mag)	r (mag)	t_{exp} (minutes)	Slit (arcsec)	S/N 4500 Å	S/N 6500 Å	v_{hel} (km s^{-1})	$\sigma(v)$ (km s^{-1})	N_{ord}	v_{AAT} (km s^{-1})
ATLAS_0	2345957664457105408	00:58:40.08	−23:51:49.7	2019 Jul 27	58,691.29	16.17	15.47	20	0.7	18	35	−131.0	0.3	35	−130.8
ATLAS_1	2349268564550587904	00:48:54.95	−22:44:58.0	2018 Sep 30	58,391.07	16.90	16.32	120	0.7	18	33	−135.7	0.5	33	−137.0
ATLAS_12	5022844307121290752	01:40:08.67	−29:52:14.6	2018 Sep 30	58,391.29	15.71	14.88	80	0.7	13	29	−84.4	0.4	19	−85.5
ATLAS_22	5039838702437479936	01:16:27.10	−26:07:01.0	2018 Oct 1	58,392.35	16.22	15.50	20	0.7	19	37	−112.1	0.5	35	−114.5
ATLAS_25	5040671754294144512	01:12:21.84	−25:44:52.2	2019 Jul 28	58,692.26	16.56	15.92	56	0.7	22	45	−116.7	0.2	35	−115.9
ATLAS_26	5040976937490509184	01:11:13.03	−24:44:48.3	2019 Jul 27	58,691.31	16.43	15.83	35	0.7	23	43	−118.7	0.2	34	−118.5
ATLAS_27	2346224467824940544	00:52:59.32	−22:54:15.5	2018 Oct 1	58,392.07	16.73	16.12	35	0.7	17	31	−142.2	0.4	34	−130.6
AliqaUma_0	4953695608534281088	02:35:26.13	−37:22:30.2	2019 Oct 19	58,775.29	17.37	16.80	120	1.0	17	29	−16.1	0.7	17	−20.4
AliqaUma_5	4966915105554905344	02:26:26.20	−35:22:26.1	2018 Oct 1	58,392.29	16.19	15.34	23	0.7	23	46	−22.6	0.3	35	−23.3
AliqaUma_7	4969961611757057536	02:16:18.92	−34:06:22.9	2019 Jul 28	58,692.34	17.03	16.45	90	0.7	27	49	−47.3	0.3	34	−35.2
AliqaUma_9	4971176778264340352	02:09:08.30	−32:46:06.1	2018 Oct 1	58,392.30	16.10	15.30	25	0.7	24	47	−50.9	0.2	33	−52.4
AliqaUma_10	4971328167270778496	02:09:58.92	−32:05:40.0	2018 Oct 1	58,392.37	16.58	15.85	28	0.7	18	35	−52.8	0.3	35	−56.5
Chenab_10	6558441247408890240	21:48:16.11	−52:11:43.8	2019 Jul 26	58,690.15	16.34	15.42	39	0.7	24	54	−147.9	0.3	35	−148.2
Chenab_12	6558460660661091456	21:46:14.54	−52:01:06.6	2019 Jul 28	58,692.08	16.36	15.26	72	0.7	20	53	−146.6	0.3	35	−148.3
Chenab_16	6559165825572005120	21:54:15.45	−49:38:05.0	2019 Jul 27	58,691.11	17.15	16.43	80	0.7	20	42	−159.3	0.3	35	−159.4
Elqui_0	4935696500108507776	01:23:24.63	−43:33:20.0	2019 Jul 26	58,690.34	17.21	16.22	81	0.7	19	49	45.3	0.5	35	+44.6
Elqui_1	4983776837921214336	01:19:05.70	−42:07:20.1	2018 Oct 1	58,392.10	16.57	15.53	49	0.7	22	54	−13.3	0.3	34	−14.6
Elqui_3	4984107138085841664	01:21:23.11	−42:02:09.2	2018 Oct 1	58,392.32	17.41	16.42	40	0.7	15	35	21.5	0.6	10	+19.9
Elqui_4	4984799005777773952	01:12:21.84	−41:33:23.9	2018 Oct 1	58,392.12	17.39	16.60	60	0.7	19	39	−16.3	0.2	33	−19.6
Indus_0	6390575508661401216	23:24:01.75	−64:02:20.8	2019 Jul 27	58,691.16	16.20	15.60	50	0.7	25	47	−28.8	0.2	34	−28.7
Indus_6	6394607108562733440	22:56:57.69	−62:41:37.5	2019 Jul 25	58,689.28	17.17	16.64	90	0.7	21	40	−24.5	0.3	35	−18.2
Indus_8	6407002315459841152	22:43:18.18	−60:54:22.5	2019 Jul 26	58,690.21	17.37	16.83	120	0.7	22	41	−42.4	0.3	13	−43.1
Indus_12	6411531547451908480	22:11:27.25	−58:04:44.7	2019 Jul 26	58,690.25	15.45	14.70	25	0.7	24	49	−56.2	0.3	35	−58.3
Indus_13	6412626111276193920	22:05:30.97	−56:30:53.4	2019 Jul 25	58,689.23	17.05	16.46	86	0.7	23	43	−58.0	0.3	35	−60.2
Indus_14	6412885389863009152	22:00:10.50	−56:04:10.3	2019 Jul 26	58,690.18	16.64	16.01	40	0.7	22	42	−65.7	0.3	35	−67.2
Indus_15	6461006409605852416	21:54:09.09	−55:18:35.0	2019 Jul 28	58,692.15	16.94	16.30	55	0.7	21	40	−61.1	0.3	35	−62.9
Jhelum_0	6502308120794799616	23:12:15.12	−51:09:36.6	2019 Jul 26	58,690.30	16.38	15.81	51	0.7	24	43	−8.2	0.3	34	−10.1
Jhelum2_2	6501458404465460992	23:18:34.74	−52:02:10.2	2019 Jul 28	58,692.24	16.15	15.53	36	0.7	24	45	−28.6	0.2	34	−16.0
Jhelum1_5	6511949016704646272	22:16:19.56	−50:00:21.1	2019 Jul 26	58,690.28	16.06	15.45	35	0.7	23	43	−23.4	0.3	34	−24.8
Jhelum1_8	6513867905012445696	22:41:59.04	−50:13:01.8	2019 Jul 27	58,691.20	16.70	16.17	60	0.7	23	41	−22.3	0.6	33	−24.5
Jhelum2_10	6514001358235953280	22:48:24.41	−50:19:51.6	2019 Jul 25	58,689.18	16.50	15.93	60	0.7	25	46	−29.7	0.3	35	−30.7
Jhelum2_11	6516771371624716288	22:36:30.00	−50:24:42.3	2019 Jul 27	58,691.25	16.69	16.16	60	0.7	23	41	−57.5	0.3	34	−58.7
Jhelum2_14	6562728071447798784	21:41:13.45	−47:29:02.0	2019 Jul 25	58,689.10	16.43	15.88	60	0.7	23	44	−118.8	0.3	34	−118.0
Jhelum2_15	6563842426481787264	21:33:27.15	−46:06:32.6	2019 Jun 24	58,658.21	15.86	15.24	64	0.7	23	43	−130.5	0.3	28	−130.7
Phoenix_1	4914426859986001920	01:23:48.36	−53:57:27.4	2018 Oct 1	58,392.18	16.98	16.39	50	0.7	23	39	63.1	0.3	33	+66.3
Phoenix_2	4914446067079706624	01:24:36.27	−53:40:01.2	2019 Oct 19	58,775.20	17.65	17.12	120	0.7	13	21	60.9	0.6	26	+59.2
Phoenix_3	4914527911976567424	01:25:55.15	−53:17:35.1	2019 Jul 25	58,689.34	17.57	17.05	120	0.7	22	40	59.1	0.4	32	+59.2
Phoenix_6	4917862490225433984	01:39:20.84	−49:09:11.7	2018 Sep 30	58,391.16	15.96	15.30	90	1.0	16	29	49.7	0.3	28	+48.4
Phoenix_7	4954034292475361280	01:42:44.22	−47:29:05.2	2018 Oct 1	58,392.25	16.28	15.65	30	0.7	26	46	40.9	0.2	13	+40.8
Phoenix_8	4954245123830234240	01:41:53.37	−47:06:51.6	2019 Jul 27	58,691.34	17.71	17.20	120	0.7	21	38	33.1	0.4	31	+35.8
Phoenix_9	4955727815260641408	01:48:16.06	−44:20:53.8	2018 Oct 1	58,392.21	16.99	16.43	40	0.7	20	35	31.2	0.3	31	+28.2
Phoenix_10	4956084950380306816	01:51:02.50	−43:02:41.0	2018 Sep 30	58,391.23	16.64	16.12	134	1.0	24	43	29.2	0.6	26	+29.5

MIKE, respectively. Data from each run were reduced with CarPy (Kelson 2003) and coadded separately.

Radial velocities for each star were measured by combining velocity measurements for individual echelle orders of both MIKE arms. Only orders 51–88 were considered, i.e., those with central wavelengths between 4000 and 6800 Å. The two bluest orders of the red arm were discarded due to low signal-to-noise ratio (S/N). Each order was normalized, and the velocity was found using a weighted cross-correlation against a high-S/N spectrum of HD 122563. This yielded a velocity and error for each order. Orders with velocities more than five biweight scales away from the biweight average were iteratively σ-clipped to remove outliers. The final velocity is an inverse-variance weighted mean of the remaining order velocities, and we adopt the weighted standard deviation as the velocity error estimate. Table 1 shows the final heliocentric velocity, velocity uncertainty, and number of orders used to measure the velocity.

While the quoted velocity uncertainties represent the achievable precision, the uncertainties are likely larger due to systematic effects. For instance, in some cases, there were up to 1 km s^{-1} offsets in the wavelength calibration between the blue and red arms of the spectrograph. There were also sometimes trends in the velocities with wavelength, suggesting that the atmospheric dispersion corrector did not completely remove the effect. The maximum size of this range is three times the quoted $\sigma(v)$ for all stars, so we recommend any statistical investigation of velocities (e.g., for binarity) inflate the errors by that amount if not investigating the detailed systematic effects.

A few stars (Jhelum2_15, Phoenix_6, and Phoenix_10) were observed on multiple runs. After measuring the velocities separately, there was no clear evidence for velocity variations. In all cases, most of the signal for the spectrum came from only one of the runs, and for clarity, we report the observed date and MJD just for that run in Table 1. The velocity for these stars is a weighted average of the individual epochs.

Figure 1 shows the difference between our MIKE velocities and the S^5 AAT velocities (Li et al. 2019). The AAT spectra were visually inspected to ensure good-quality velocity measurements, and the velocity precision is 0.7–1.7 km s^{-1} for all stars. Three (eight) stars have velocity differences larger than 5σ (3σ), suggesting that these stars are likely (possible) binaries. After removing the eight possible binaries, the median velocity offset is -1.21 km s^{-1}, similar in magnitude to the -1.11 km s^{-1} global offset applied to the original `rvspecfit` velocities to match the absolute scale of APOGEE and Gaia. Changing between 5σ and 3σ binary candidates affects this offset by less than 0.05 km s^{-1}. Since the absolute scale is uncertain, this offset is not applied in Table 1, but any comparisons between the MIKE and AAT velocities should account for this.

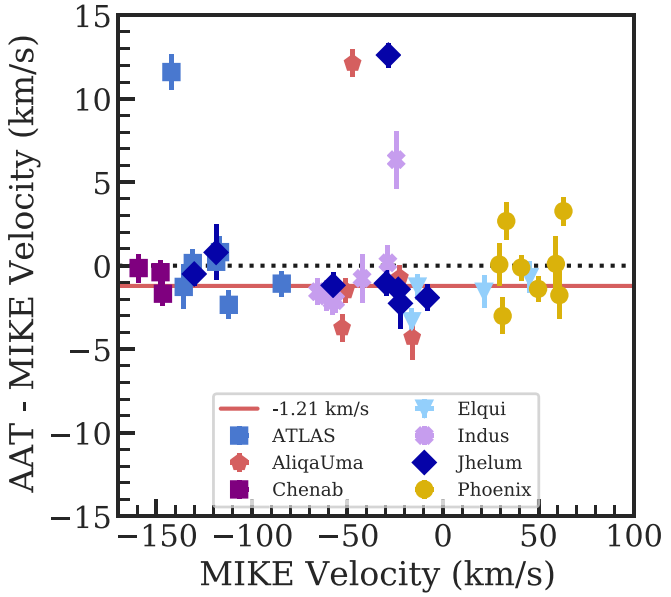

Figure 1. Difference between S^5 AAT (Li et al. 2019) and MIKE velocities. After removing binaries, the remaining median offset is -1.21 km s^{-1}, indicated by the red line.

3. Stellar Parameters

The effective temperature $T_{\rm eff}$ was determined photometrically using a dereddened $g-r$ color and color–temperature relations derived from the Dartmouth isochrones (Dotter et al. 2008). The photometry was from the DES Data Release 1 (DR1) with the color excess $E(B-V)$ from Schlegel et al. (1998) and the extinction coefficients from DES DR1 (DES Collaboration et al. 2018), namely,

$$g_0 = g - 3.186E(B-V)_{\rm SFD}, \quad (1)$$

$$r_0 = r - 2.140E(B-V)_{\rm SFD}. \quad (2)$$

The photometric uncertainties for our relatively bright stars are dominated by systematics, and we assume a 0.02 mag color uncertainty for all of our stars that can be attributed to reddening error. The photometry was converted to a temperature by comparing to 12 Gyr α-enhanced Dartmouth isochrones with [Fe/H] $= -2.5$, -2.0, and -1.5. Using the isochrone with the closest predicted g magnitude, $g-r$ was converted to $T_{\rm eff}$. The difference between the other isochrones was added to the $T_{\rm eff}$ uncertainty, along with propagating the 0.02 mag color uncertainty. Together, the typical $T_{\rm eff}$ uncertainty is 50–60 K. At this level of uncertainty, using different old ages (10–14 Gyr) or α-normal isochrones makes a negligible extra difference to the derived temperatures.

Surface gravity $\log g$ was determined photometrically from the DES g magnitude using the equation (Venn et al. 2017)

$$\log g = 4.44 + \log M_\star + 4\log(T_{\rm eff}/5780\ {\rm K}) + 0.4(g_0 - \mu + {\rm BC}(g) - 4.75). \quad (3)$$

The Casagrande & VandenBerg (2014) bolometric corrections (BC(g)) were used for SDSS magnitudes, which are not significantly different from DES magnitudes for this purpose. All stars were assumed to have mass $M_\star = 0.75 \pm 0.1\ M_\odot$, as typical for an old red giant. The distance moduli μ were assumed to be constant for each stream, using the values from Shipp et al. (2018). Since some streams exhibit significant distance gradients up to 0.3 mag (Li et al. 2020), we assume a 1σ distance modulus uncertainty of 0.3 mag. The final $\log g$ uncertainty is derived by propagating individual uncertainties in Equation (3) and dominated by the distance modulus uncertainty. The typical $\log g$ uncertainty is 0.16 dex.

After fixing $T_{\rm eff}$ and $\log g$ and measuring equivalent widths, the microturbulence ν_t was determined for each star by balancing the abundance of Fe II lines versus their reduced equivalent width. We used Fe II instead of Fe I because all of our stars have at least eight Fe II lines spanning a wide range of line strengths (typically $-5.4 < \log {\rm EQW}/\lambda < -4.6$, while Fe I lines spanned $-5.4 < \log {\rm EQW}/\lambda < -4.5$), and using photometric temperatures has a significant impact on the microturbulence derived from Fe I lines. This is because an LTE analysis using photometric temperatures will not satisfy excitation equilibrium, and there are correlations between excitation potential and reduced equivalent width. Using Fe I instead of Fe II typically results in $\approx 0.3\,{\rm km\,s^{-1}}$ higher microturbulence. The ν_t uncertainty is estimated by varying ν_t until the slope changes by one standard error on the slope. The typical ν_t uncertainty is $0.21\,{\rm km\,s^{-1}}$, though in two stars, it was as high as $\sim 0.6\,{\rm km\,s^{-1}}$. Those stars have lower S/Ns, resulting in relatively few ($\sim$10) noisier Fe II lines that do not span as wide a range of reduced equivalent widths.

The model metallicity was set to match the simple average of the Fe II lines, and $[\alpha/{\rm Fe}] = +0.4$ unless [Mg/Fe] was significantly lower. We used $[\alpha/{\rm Fe}] = +0.0$ for Elqui_3 and Elqui_4, $[\alpha/{\rm Fe}] = +0.2$ for Elqui_0 and AliqaUma_0, and $[\alpha/{\rm Fe}] = +0.1$ for Jhelum2_14. A model metallicity uncertainty of 0.2 dex was adopted for all stars. The $[\alpha/{\rm Fe}]$ and [M/H] values used do not affect the abundances nearly as much as the temperature, surface gravity, and microturbulence.

The resulting stellar parameters are given in Table 2 and plotted in Figure 2. The top panel shows $T_{\rm eff}$ versus $\log g$ for our stars, which are well matched to the Dartmouth isochrones. The bottom panel shows ν_t versus $\log g$ for our stars, which lie near empirical fits to other high-resolution samples (Barklem et al. 2005; Marino et al. 2008; Kirby et al. 2009). In general, the results are well matched to the Barklem et al. (2005) fit, as expected, since this fit was derived using the largest number of cool and metal-poor giants.

The stellar parameters are compared to a standard 1D LTE spectroscopic analysis and the AAT spectra analyzed by `rvspecfit` in Appendix A, finding good agreement after accounting for expected systematic uncertainties. It is clear there are no foreground dwarf stars in our sample, validating the use of photometric stellar parameters.

Table 2
Stellar Parameters

Star	$T_{\rm eff}$ (K)	$\log g$ (dex)	ν_t (km s^{-1})	[M/H]
AliqaUma_0	5131 ± 62	1.97 ± 0.16	2.31 ± 0.26	−2.40
AliqaUma_10	4785 ± 39	1.45 ± 0.16	1.75 ± 0.18	−2.28
AliqaUma_5	4575 ± 55	1.13 ± 0.16	1.87 ± 0.19	−2.34
AliqaUma_7	5092 ± 58	1.82 ± 0.16	1.90 ± 0.17	−2.37
AliqaUma_9	4618 ± 52	1.14 ± 0.16	2.06 ± 0.17	−2.46
ATLAS_0	4833 ± 41	1.52 ± 0.16	1.92 ± 0.23	−2.47
ATLAS_1	5088 ± 57	1.97 ± 0.16	2.06 ± 0.23	−2.43
ATLAS_12	4590 ± 54	1.16 ± 0.16	2.20 ± 0.55	−2.16
ATLAS_22	4781 ± 44	1.51 ± 0.16	1.70 ± 0.17	−2.18
ATLAS_25	4937 ± 43	1.75 ± 0.16	1.84 ± 0.25	−2.36
ATLAS_26	5042 ± 47	1.75 ± 0.16	1.91 ± 0.16	−2.26
ATLAS_27	5002 ± 44	1.86 ± 0.16	2.33 ± 0.42	−2.55
Chenab_10	4528 ± 63	0.85 ± 0.17	2.23 ± 0.16	−1.94
Chenab_12	4263 ± 57	0.62 ± 0.17	2.44 ± 0.21	−1.80
Chenab_16	4819 ± 41	1.41 ± 0.16	1.95 ± 0.18	−2.15
Elqui_0	4374 ± 75	0.91 ± 0.17	2.27 ± 0.20	−2.02
Elqui_1	4316 ± 54	0.56 ± 0.17	2.41 ± 0.25	−2.91
Elqui_3	4380 ± 74	0.99 ± 0.17	2.32 ± 0.29	−1.81
Elqui_4	4645 ± 50	1.20 ± 0.16	2.13 ± 0.15	−2.03
Indus_0	5040 ± 47	1.93 ± 0.16	1.73 ± 0.23	−2.41
Indus_12	4741 ± 46	1.45 ± 0.16	1.90 ± 0.20	−2.14
Indus_13	5063 ± 58	2.29 ± 0.16	1.59 ± 0.16	−1.91
Indus_14	4969 ± 51	2.08 ± 0.16	1.52 ± 0.22	−1.98
Indus_15	4937 ± 52	2.18 ± 0.16	1.59 ± 0.14	−1.71
Indus_6	5251 ± 66	2.43 ± 0.16	1.73 ± 0.34	−2.45
Indus_8	5206 ± 65	2.50 ± 0.16	1.66 ± 0.21	−2.02
Jhelum_0	5122 ± 58	2.27 ± 0.16	1.63 ± 0.19	−2.02
Jhelum1_5	5011 ± 53	2.07 ± 0.16	1.67 ± 0.15	−2.12
Jhelum1_8	5199 ± 66	2.44 ± 0.16	1.52 ± 0.21	−2.42
Jhelum2_10	5116 ± 58	2.31 ± 0.16	1.47 ± 0.17	−2.01
Jhelum2_11	5220 ± 65	2.44 ± 0.16	1.67 ± 0.25	−2.17
Jhelum2_14	5188 ± 66	2.31 ± 0.16	1.73 ± 0.26	−2.48
Jhelum2_15	5001 ± 52	1.98 ± 0.16	1.68 ± 0.21	−2.14
Jhelum2_2	4967 ± 51	2.09 ± 0.16	1.49 ± 0.22	−1.62
Phoenix_1	5088 ± 57	2.15 ± 0.16	1.47 ± 0.19	−2.52
Phoenix_10	5279 ± 68	2.12 ± 0.16	1.80 ± 0.33	−2.93
Phoenix_2	5252 ± 66	2.51 ± 0.16	1.64 ± 0.30	−2.67
Phoenix_3	5272 ± 67	2.49 ± 0.16	1.49 ± 0.38	−2.76
Phoenix_6	4905 ± 43	1.64 ± 0.16	2.11 ± 0.59	−2.68
Phoenix_7	4980 ± 45	1.82 ± 0.16	1.58 ± 0.18	−2.62
Phoenix_8	5292 ± 71	2.56 ± 0.17	1.53 ± 0.07	−2.79
Phoenix_9	5153 ± 64	2.20 ± 0.16	1.55 ± 0.27	−2.70

Note. All [M/H] errors are taken to be 0.2 dex.

4. Abundance Analysis

A standard abundance analysis was performed with the 2017 version of the 1D LTE radiative transfer code `MOOG` that includes scattering (Sneden 1973; Sobeck et al. 2011)[24] and the `ATLAS` model atmospheres (Castelli & Kurucz 2003). The analysis code `SMHR`[25] (first described in Casey 2014) was used to measure equivalent widths, interpolate model atmospheres, run `MOOG`, and fit syntheses. We have implemented a new error analysis formalism in `SMHR` that is described in Appendix B.

4.1. Atomic Data

The baseline lists are adapted from `linemake`.[26] These start with the Kurucz line lists (Kurucz & Bell 1995),[27] then replace individual lines with those from laboratory measurements (summaries in Sneden et al. 2009 for neutron-capture elements; Sneden et al. 2016 for iron-peak elements). The most recent update is to Fe II lines (Den Hartog et al. 2019). We also used NIST to update many light elements (sodium, magnesium, aluminum, silicon, and potassium; Kramida et al. 2019); VALD to update calcium lines (Ryabchikova et al. 2015); and Caffau et al. (2008) for the oxygen lines. For molecular lines, the default Kurucz CH lists were replaced with those from Masseron et al. (2014), and the CN lists are from Sneden et al. (2014). Any hyperfine splitting is also taken from `linemake`. Atomic data and references are given in Table 3.

For future reference, we recommend using the Sc II $\log gf$ and hyperfine structure (hfs) from Lawler et al. (2019), rather than the older Lawler & Dakin (1989) values. This choice does not affect our results because only UV lines and the 5700 Å multiplet have significant differences in Lawler et al. (2019), and we did not use any of those lines. The oscillator strengths

[24] https://github.com/alexji/moog17scat
[25] https://github.com/andycasey/smhr
[26] https://github.com/vmplacco/linemake
[27] http://kurucz.harvard.edu/linelists.html

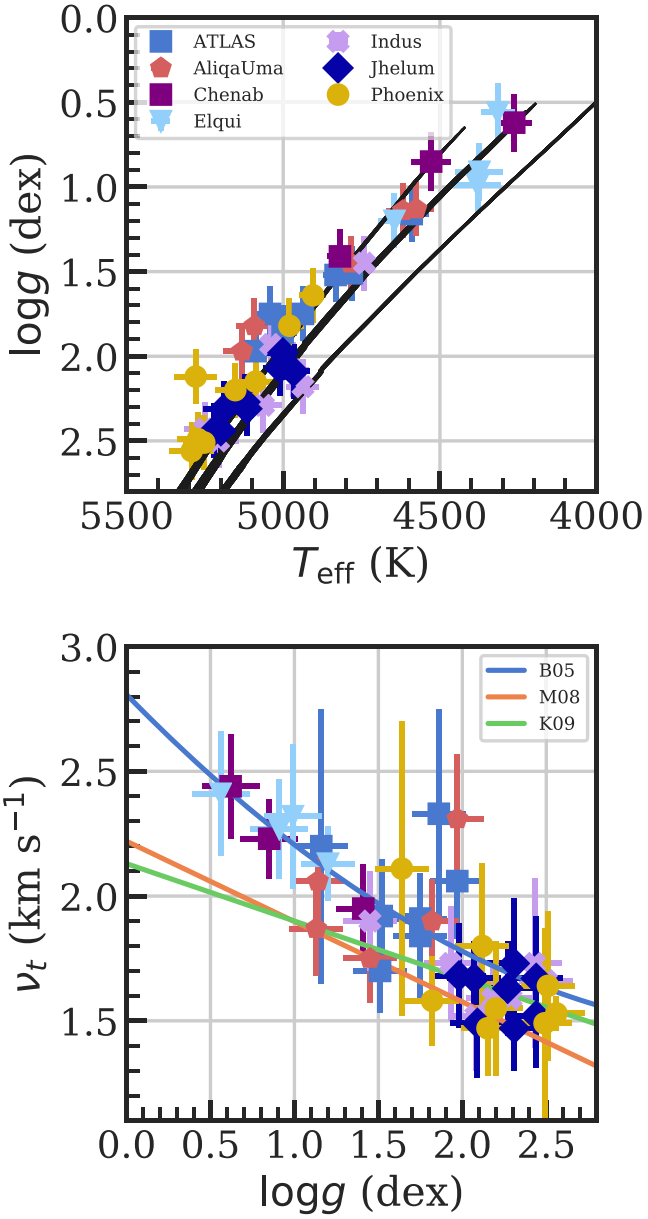

Figure 2. Stellar parameters for all analyzed stars compared to scaling relations. The top panel shows $T_{\rm eff}$ vs. log g compared to Dartmouth isochrones of three different metallicities ([Fe/H] = −2.5, −2.0, −1.5). Isochrones of different ages and α-enhancements have also been plotted, but they are essentially identical for these red giants. The bottom panel shows log g vs. ν_t compared to three empirical log g-to-ν_t fits (Barklem et al. 2005; Marino et al. 2008; Kirby et al. 2009).

for the lines we used differ by no more than 0.03 dex in the updated data, within the measurement uncertainty.

For Ba and Eu, r-process isotopes were assumed (Sneden et al. 2008), and $^{12}C/^{13}C = 9$. These choices and their impact are discussed in Section 6.

4.2. Equivalent Widths

Equivalent widths were measured semiautomatically using SMHR. Each absorption line was fit with a model that includes a (usually Gaussian, sometimes Voigt; see Section 6) absorption profile multiplied by a linear continuum model. After these parameters are optimized, the algorithm identifies groups (>3) of neighboring pixels that are significantly discrepant (>3σ) from the fitted model and tries to improve the fit by including an absorption profile centered on the group with the profile width matched to the absorption line of interest. This procedure occurs iteratively and minimizes the effects of nearby absorption lines biasing the local continuum determination. After this, all measurements were manually inspected to verify each line, primarily to add extra masks as necessary or reject lines with reduction artifacts. The final equivalent width uncertainties include continuum placement uncertainty.

To verify the equivalent widths from SMHR, we also independently measured equivalent widths using IRAF[28] in two-thirds of our target stars. The differences are consistent with spectrum noise and described in Appendix C.

Table 3
Atomic Data

Elem.	Wave	ExPot	log gf	References
C–H	4310.00	⋯	⋯	(1)
C–H	4323.00	⋯	⋯	(1)
C–N	3876.00	⋯	⋯	(2)
O I	6300.30	0.00	−9.82	(3)
O I	6363.78	0.02	−10.30	(3)
Na I	5682.63	2.10	−0.71	(4)
Na I	5688.20	2.10	−0.41	(4)

References. (1) Masseron et al. (2014); (2) Sneden et al. (2014); (3) Caffau et al. (2008); (4) Kramida et al. (2019); (5) Ryabchikova et al. (2015); (6) Lawler & Dakin (1989), using hfs from Kurucz & Bell (1995); (7) Lawler et al. (2013); (8) Wood et al. (2013); (9) Lawler et al. (2014); (10) Wood et al. (2014a); (11) Sobeck et al. (2007); (12) Lawler et al. (2017); (13) Den Hartog et al. (2011); (14) Belmonte et al. (2017); (15) Den Hartog et al. (2014); (16) O'Brian et al. (1991); (17) Ruffoni et al. (2014); (18) Meléndez & Barbuy (2009); (19) Den Hartog et al. (2019); (20) Lawler et al. (2015); (21) Wood et al. (2014b); (22) Roederer & Lawler (2012); (23) Biémont et al. (2011); (24) Hannaford et al. (1982); (25) Ljung et al. (2006); (26) McWilliam (1998); (27) Lawler et al. (2001a); (28) Lawler et al. (2009); (29) Den Hartog et al. (2003); (30) Lawler et al. (2006); (31) Lawler et al. (2001b); (32) Den Hartog et al. (2006); (33) Sneden et al. (2009).

(This table is available in its entirety in machine-readable form.)

4.3. Syntheses

Abundances of synthesized lines were automatically fit using SMHR. The fitting algorithm does a χ^2 minimization jointly optimizing the abundance of one element, the local continuum (which is usually a linear model), a Gaussian smoothing kernel, and a radial velocity offset that is bounded to be small. To reduce the number of MOOG calls, local grids of spectra are synthesized and linearly interpolated within this grid during optimization. Each fit was visually examined, and poor-fitting spectral regions were masked and refit. The final abundance uncertainties include the uncertainty in the local continuum fit, smoothing, and radial velocity. To verify our results, we also independently synthesized lines for stars spanning the S/N and stellar parameter range. The differences are mostly consistent with noise and described in Appendix C. For a few elements (Al, Sc, Mn, and Ba), this verification suggests that the synthesis statistical uncertainties are not sufficient to describe

[28] IRAF is distributed by the National Optical Astronomy Observatory, which is operated by the Association of Universities for Research in Astronomy (AURA) under a cooperative agreement with the National Science Foundation.

the spectrum noise. An extra systematic uncertainty is added in quadrature for these elements (described in detail in Section 6).

4.4. Upper Limits

Upper limits were derived with spectral synthesis following the procedure in Ji et al. (2020). For each feature, a synthetic spectrum was fit to match the continuum, radial velocity, and smoothing of the observed spectrum. Then, holding the continuum and smoothing fixed, the abundance was increased until $\Delta\chi^2 = 25$. This is formally a 5σ upper limit, though it does not include uncertainties for the continuum placement. While this works well for individual isolated lines, the provided upper limits for molecular features CH and CN are likely overconfident because they do not account for continuum placement.

4.5. Combining Lines and Error Analysis

We have applied a new method to combine individual line measurements and uncertainties in a way that fully and self-consistently propagates statistical and stellar parameter uncertainties for individual line measurements. A full derivation and justification are described in Appendix B, but the procedure is described here.

For a given star, let each species X have N lines indexed by $i = 1, \ldots, N$. Each line has a measured abundance x_i (in units of $\log\epsilon\,(\mathrm{X})$), statistical uncertainty e_i, and stellar parameter differences $\delta_{i,k}$ where k is one of the stellar parameters $T_{\rm eff}$, $\log g$, ν_t, or [M/H]. Additionally, each species X has a systematic uncertainty $s_{\rm X} \geqslant 0$, such that the total uncertainty on an individual line is $\sigma_i^2 = e_i^2 + s_{\rm X}^2$. Rather than directly combining the lines (e.g., with a straight or inverse-variance weighted average), we now include the fact that the lines x_i are correlated due to stellar parameters.

The stellar parameters $\theta = (T_{\rm eff}, \log g, \nu_t, [\mathrm{M/H}])$ are drawn from a multivariate distribution with covariance matrix Σ_θ. We construct this, noting that $\Sigma_{\theta,kl} = \sigma_k\sigma_l\rho_{kl}$, where σ_k and σ_l are individual stellar parameter uncertainties (from Table 2), and ρ_{kl} is the correlation matrix between these parameters (e.g., McWilliam et al. 2013):

$$\rho = \begin{pmatrix} 1 & \rho_{T_{\rm eff},\log g} & \rho_{T_{\rm eff},\nu_t} & \rho_{T_{\rm eff},[\mathrm{M/H}]} \\ \rho_{T_{\rm eff},\log g} & 1 & \rho_{\log g,\nu_t} & \rho_{\log g,[\mathrm{M/H}]} \\ \rho_{T_{\rm eff},\nu_t} & \rho_{\log g,\nu_t} & 1 & \rho_{\nu_t,[\mathrm{M/H}]} \\ \rho_{T_{\rm eff},[\mathrm{M/H}]} & \rho_{\log g,[\mathrm{M/H}]} & \rho_{\nu_t,[\mathrm{M/H}]} & 1 \end{pmatrix}. \quad (4)$$

Since our data are a reasonably large sample of metal-poor red giants, the stellar parameter correlations ρ were estimated by taking the Pearson correlation of our stars' parameters using `scipy.stats.pearsonr`, reported in Table 4. The strong correlation between $T_{\rm eff}$ and $\log g$ matches other isochrone-based determinations (McWilliam et al. 2013).

With these values, the $N \times N$ covariance matrix is constructed with

$$\widetilde{\Sigma} = \mathrm{diag}(\sigma_i^2) + \delta\rho\delta^T, \quad (5)$$

where δ is the $N \times 4$ matrix of $\delta_{i,k}$, and δ^T is the transposed matrix. The matrix is then inverted to calculate an effective weight for each line:

$$\widetilde{w}_i = \sum_j \Sigma_{ij}^{-1}. \quad (6)$$

Note that the individual $\widetilde{w}_i$ can be negative, but the sum $\sum_i \widetilde{w}_i$ is always positive. Also, $\widetilde{w}_i$ must be recomputed if using a subset of lines. Then the best estimate $\hat{x}$ of the average abundance of X, accounting for all stellar parameter correlations and statistical uncertainties, is

$$\hat{x} = \frac{\sum_i \widetilde{w}_i x_i}{\sum_i \widetilde{w}_i}, \quad (7)$$

while the variance on $\hat{x}$ is given by

$$\mathrm{Var}(\hat{x}) = \frac{1}{\sum_i \widetilde{w}_i} \quad (8)$$

and the error on X is $\sqrt{\mathrm{Var}(\hat{x})}$.

Table 4
Stellar Parameter Correlations

Variables	Value
$\rho_{T_{\rm eff},\log g}$	+0.96
$\rho_{T_{\rm eff},\nu_t}$	−0.82
$\rho_{T_{\rm eff},[\mathrm{M/H}]}$	−0.37
$\rho_{\log g,\nu_t}$	−0.87
$\rho_{\log g,[\mathrm{M/H}]}$	−0.21
$\rho_{\nu_t,[\mathrm{M/H}]}$	+0.01

Table 5 contains all of the individual line measurements. For each line i, it has the line abundance $\log\epsilon_i = x_i$; all of the statistical (e_i), systematic ($s_{\rm X}$), and stellar parameter ($\delta_{i,k}$) errors needed to compute $\widetilde{\Sigma}$ and $\widetilde{w}$; and the actual value of $\widetilde{w}_i$ for each line. In the example table, two Fe I lines that have opposite signs for $\widetilde{w}$ are shown. This means that stellar parameters have a differential effect on the lines relative to the mean abundance. In this case, one Fe line is much stronger than the other, so errors in microturbulence have a substantial differential effect that causes the different signs. The table also has an example of three Mg I lines with very different weights. The 4703 Å line counts much more because it has a significantly lower statistical uncertainty and moderately less dependence on stellar parameters. The 5172 Å line has almost no weight because it is near saturation, and a small equivalent error corresponds to a large abundance error. This illustrates one major benefit of including line-by-line uncertainties, i.e., that known dependencies on stellar parameters and S/N are automatically taken into account. The final abundances are thus much less dependent on the specific set of lines chosen for abundance measurements.

The final combined abundances are tabulated in Table 6; $\log\epsilon$ is the result of Equation (7). The standard spectroscopic notation $[\mathrm{X/H}] = \log\epsilon\,(\mathrm{X}) - \log\epsilon_\odot(\mathrm{X})$ is normalized using solar abundances from Asplund et al. (2009). Uncertainties in the solar normalization were not propagated, so the [X/H] uncertainties are the same as the $\log\epsilon$ uncertainties. $\sigma_{[\mathrm{X/H}]}$ is the result of Equation (8).

The [X/Fe] values have two complications: a choice must be made between Fe I and Fe II, and correlated uncertainties in X and Fe must be propagated. By default in this paper, we have

Table 5
Line Measurements

Star	λ	ID	χ	$\log gf$	EW	σ(EW)	FWHM	ul	$\log \epsilon_i$	σ_i	e_i	s_X	$\delta_{i,T_{\rm eff}}$	$\delta_{i,\log g}$	δ_{i,ν_t}	$\delta_{i,[M/H]}$	$\widetilde{w}_i$
ATLAS_1	4702.99	12.0	4.35	−0.44	85.7	3.9	0.17		5.56	0.06	0.06	0.00	+0.04	−0.02	−0.04	+0.00	121.19
ATLAS_1	5172.68	12.0	2.71	−0.39	194.9	38.4	0.30		5.37	0.30	0.30	0.00	+0.07	−0.06	−0.08	−0.00	1.08
ATLAS_1	5227.19	26.0	1.56	−1.23	139.7	9.4	0.25		5.62	0.30	0.18	0.24	+0.09	−0.03	−0.19	−0.02	−4.86
ATLAS_1	5250.65	26.0	2.20	−2.18	50.8	6.1	0.13		5.53	0.26	0.10	0.24	+0.06	−0.00	−0.03	+0.00	6.39
ATLAS_1	5528.40	12.0	4.35	−0.50	92.1	6.8	0.24		5.70	0.10	0.10	0.00	+0.04	−0.01	−0.05	+0.00	26.70
ATLAS_1	4310.00	106.0	⋯	⋯	syn	syn	0.14		6.43	0.10	0.10	0.00	+0.12	−0.06	+0.00	+0.05	64.05
ATLAS_1	4041.35	25.0	2.11	0.28	syn	syn	⋯	<	3.53	⋯	⋯	⋯	⋯	⋯	⋯	⋯	⋯

(This table is available in its entirety in machine-readable form.)

Table 6
Stellar Abundances

Star	El.	N	ul	$\log\epsilon$	[X/H]	$\sigma_{[X/H]}$	[X/Fe]	$\sigma_{[X/Fe]}$	Δ_T	Δ_g	Δ_v	Δ_M	s_X
ATLAS_1	C–H	2		+6.43	−2.00	0.09	+0.41	0.10	0.11	−0.06	0.01	0.05	0.00
ATLAS_1	C–N	1	<	+6.21	−1.62	⋯	+0.78	⋯	⋯	⋯	⋯	⋯	⋯
ATLAS_1	O I	1	<	+8.18	−0.51	⋯	+1.89	⋯	⋯	⋯	⋯	⋯	⋯
ATLAS_1	Na I	2		+4.45	−1.79	0.13	+0.61	0.12	0.08	−0.06	−0.09	−0.01	0.00
ATLAS_1	Mg I	6		+5.60	−2.00	0.07	+0.40	0.08	0.04	−0.02	−0.04	0.00	0.00
ATLAS_1	Al I	2		+3.10	−3.35	0.50	−0.95	0.50	0.11	−0.04	−0.06	0.02	0.59
ATLAS_1	Si I	2		+5.76	−1.75	0.14	+0.66	0.15	0.02	−0.04	−0.06	0.01	0.00
ATLAS_1	K I	2		+3.40	−1.63	0.10	+0.77	0.10	0.05	−0.01	−0.03	−0.00	0.00
ATLAS_1	Ca I	16		+4.29	−2.05	0.08	+0.35	0.09	0.04	−0.00	−0.03	−0.00	0.17
ATLAS_1	Sc II	7		+0.72	−2.43	0.10	+0.05	0.10	0.01	0.04	−0.01	0.01	0.10
ATLAS_1	Ti I	11		+2.92	−2.03	0.09	+0.38	0.09	0.06	−0.01	−0.01	0.00	0.00
ATLAS_1	Ti II	26		+2.91	−2.04	0.09	+0.44	0.10	0.02	0.05	0.01	0.02	0.21
ATLAS_1	V I	1		+1.75	−2.18	0.12	+0.22	0.13	0.02	0.02	0.01	−0.02	0.00
ATLAS_1	V II	1		+1.75	−2.18	0.21	+0.30	0.20	−0.01	0.16	0.04	0.01	0.00
ATLAS_1	Cr I	5		+3.21	−2.42	0.11	−0.02	0.11	0.06	−0.01	−0.02	−0.00	0.17
ATLAS_1	Cr II	1		+3.44	−2.20	0.10	+0.28	0.10	−0.01	0.05	−0.02	0.01	0.00
ATLAS_1	Mn I	1	<	+3.53	−1.90	⋯	+0.51	⋯	⋯	⋯	⋯	⋯	⋯
ATLAS_1	Fe I	91		+5.10	−2.40	0.06	+0.00	0.00	0.05	−0.00	0.02	0.01	0.24
ATLAS_1	Fe II	10		+5.02	−2.48	0.09	+0.00	0.00	0.00	0.05	−0.00	0.02	0.07
ATLAS_1	Co I	4		+3.00	−1.99	0.16	+0.41	0.16	0.06	0.01	−0.02	−0.01	0.15
ATLAS_1	Ni I	8		+4.07	−2.15	0.12	+0.26	0.12	0.05	−0.00	−0.01	0.00	0.28
ATLAS_1	Cu I	1	<	+2.70	−1.49	⋯	+0.92	⋯	⋯	⋯	⋯	⋯	⋯
ATLAS_1	Zn I	1	<	+2.80	−1.76	⋯	+0.65	⋯	⋯	⋯	⋯	⋯	⋯
ATLAS_1	Sr II	2		+0.20	−2.67	0.26	−0.19	0.25	−0.02	0.06	−0.10	−0.02	0.17
ATLAS_1	Y II	2		−0.26	−2.47	0.12	+0.01	0.11	0.02	0.05	−0.01	0.02	0.00
ATLAS_1	Zr II	1		+0.59	−1.99	0.22	+0.49	0.22	−0.01	0.06	−0.02	−0.01	0.00
ATLAS_1	Ba II	5		−0.51	−2.69	0.14	−0.21	0.12	0.03	0.04	−0.04	0.01	0.11
ATLAS_1	La II	1	<	+0.21	−0.89	⋯	+1.59	⋯	⋯	⋯	⋯	⋯	⋯
ATLAS_1	Eu II	2	<	−1.12	−1.64	⋯	+0.84	⋯	⋯	⋯	⋯	⋯	⋯

Note. One star from this table is shown for form. The full version is available online.

(This table is available in its entirety in machine-readable form.)

decided to use Fe I for neutral species and Fe II for ionized species (e.g., [Mg I/Fe I] or [Ti II/Fe II]). This is because neutral and ionized species usually have similar dependencies on stellar parameters, maximizing the precision on the final [X/Fe] ratio (e.g., Roederer et al. 2014). For the correlated uncertainties, first note that [X/Fe] = [X/H] − [Fe/H]. Thus, Var([X/Fe]) = Var(X) + Var(Fe) − 2Cov(X, Fe). For any two different species X and Y, the covariance in $\log\epsilon$(X) and $\log\epsilon$(Y) is given by

$$\mathrm{Cov}(\hat{x}, \hat{y}) = \Delta_X \rho \Delta_Y, \quad (9)$$

where Δ_X is a vector of the $\Delta_{X,k}$ for $k = T$, g, v, and M given in Table 6 and ρ is from Equation (4). Here Δ_X is the weighted response of species X to the stellar parameter errors in Table 2, defined in detail in Appendix B. The error $\sigma_{[X/Fe]}$ in Table 6 is then calculated using Equations (8) and (9). Note that Equation (9) is not correct if X = Y; use Equation (8) instead.

There are sometimes mild differences between [M/H] and [Fe/H] because the stellar parameter determination did not include the effect of weighted lines. However, the resulting differences in the model metallicity are much less than <0.2 dex, which is included in the error propagation. Model metallicity uncertainties also make a negligible difference in the results compared to other sources of uncertainty. In general, [Fe I/H] and [Fe II/H] agree, with a typical difference of -0.08 ± 0.11 dex, where [Fe I/H] is lower, as expected from non-LTE (NLTE) effects (e.g., Ezzeddine et al. 2017). However, four stars have particularly large differences; Elqui_0, Elqui_3, Elqui_4, and ATLAS_12 have [Fe I/H] − [Fe II/H] < −0.20 (see Section 6.5).

5. Abundance Results

Table 5 has every individual line measurement for our stars, including upper limits. Each row contains the star name, the wavelength λ of the relevant feature in Å, the MOOG species (ID), the excitation potential and $\log gf$, the equivalent width and uncertainty when available (EW, σ(EW)), the FWHM (in Å), an upper limit flag (ul), the measured abundance $\log\epsilon_i$, a total abundance uncertainty σ_i, a statistical uncertainty e_i that propagates spectrum noise, a systematic uncertainty s_X that accounts for line-to-line scatter in excess of the abundance uncertainties (see Appendix B), the stellar parameter abundance differences $\delta_{i,k}$, and an effective weight $\widetilde{w}_i$.

Table 6 has the final abundances for our stars. Each row contains the star name, the element measured (El.), the number of lines used (N), an upper limit flag (ul), the abundance ($\log\epsilon$), the [X/H] value relative to the Asplund et al. (2009) solar abundances, the uncertainty on $\log\epsilon$(X) and [X/H] that includes both statistical and stellar parameter uncertainties ($\sigma_{[X/H]}$), the [X/Fe] value and uncertainty (where Fe is Fe I if X is neutral and Fe II if X is ionized), and the abundance differences due to a 1σ change in stellar parameters Δ_k. Several important elements and their abundance uncertainties are summarized for all stars in Table 7.

Figure 3 shows most of the element abundances measured in this paper. This figure uses [Fe I/H] on the x-axis and [X/Fe]

Table 7
Abundance Summary

Star	[Fe I/H]		[Fe II/H]		[C/Fe]		[Na/Fe]		[Mg/Fe]		[Ca/Fe]		[Ti II/Fe]		[Ni/Fe]		[Sr/Fe]		[Ba/Fe]		[Eu/Fe]	
AliqaUma_0	−2.38	0.08	−2.39	0.08	−0.03	lim	⋯	⋯	+0.24	0.10	+0.25	0.10	+0.22	0.13	+0.19	0.16	−0.48	0.58	−0.24	0.14	+0.74	lim
AliqaUma_10	−2.38	0.06	−2.31	0.08	−0.13	0.11	+0.45	0.10	+0.55	0.09	+0.39	0.08	+0.27	0.09	+0.18	0.08	+0.15	0.14	−0.02	0.16	+0.32	0.09
AliqaUma_5	−2.49	0.05	−2.33	0.11	−0.36	0.17	+0.40	0.16	+0.52	0.08	+0.47	0.07	+0.23	0.09	+0.12	0.07	+0.13	0.14	−0.10	0.17	+0.28	0.09
AliqaUma_7	−2.51	0.04	−2.40	0.06	−0.30	0.10	+0.41	0.16	+0.47	0.06	+0.47	0.06	+0.46	0.07	+0.09	0.08	+0.11	0.17	+0.00	0.12	+0.33	0.08
AliqaUma_9	−2.52	0.06	−2.47	0.07	−0.24	0.14	+0.48	0.11	+0.61	0.08	+0.47	0.08	+0.18	0.09	+0.15	0.08	+0.20	0.13	+0.07	0.14	+0.30	0.07
ATLAS_0	−2.41	0.06	−2.39	0.09	−0.06	0.10	+0.49	0.11	+0.52	0.08	+0.44	0.08	+0.28	0.08	+0.11	0.07	+0.16	0.18	−0.04	0.22	+0.33	0.09
ATLAS_1	−2.40	0.06	−2.48	0.09	+0.41	0.10	+0.61	0.12	+0.40	0.08	+0.35	0.09	+0.38	0.09	+0.26	0.12	−0.19	0.25	−0.21	0.12	+0.84	lim
ATLAS_12	−2.61	0.08	−2.32	0.19	−0.20	0.17	+0.27	0.35	+0.66	0.14	+0.40	0.16	+0.33	0.18	+0.30	0.16	+0.05	0.32	−0.34	0.24	+0.18	0.21
ATLAS_22	−2.39	0.06	−2.20	0.09	−0.04	0.11	+0.61	0.08	+0.56	0.08	+0.43	0.08	+0.20	0.09	+0.12	0.10	+0.06	0.11	−0.07	0.15	+0.13	0.09
ATLAS_25	−2.44	0.04	−2.43	0.09	+0.05	0.10	+0.41	0.15	+0.44	0.08	+0.30	0.07	+0.20	0.07	+0.17	0.06	+0.22	0.18	−0.05	0.14	+0.52	0.10
ATLAS_26	−2.45	0.05	−2.29	0.07	−0.41	0.12	+0.66	0.10	+0.52	0.07	+0.43	0.07	+0.37	0.06	+0.00	0.09	+0.29	0.13	+0.06	0.14	+0.30	0.09
ATLAS_27	−2.36	0.04	−2.47	0.12	+0.30	0.09	+0.27	0.22	+0.46	0.11	+0.39	0.08	+0.24	0.10	−0.21	0.13	+0.02	0.31	−0.12	0.16	+0.46	0.20
Chenab_10	−1.94	0.07	−1.98	0.08	−0.74	0.18	+0.04	0.10	+0.45	0.09	+0.31	0.09	+0.14	0.10	−0.06	0.10	−0.47	0.16	−0.43	0.11	+0.17	0.06
Chenab_12	−1.97	0.08	−1.87	0.10	−0.50	0.21	−0.12	0.12	+0.35	0.12	+0.29	0.11	+0.35	0.14	+0.01	0.11	−0.29	0.14	−0.21	0.14	+0.29	0.08
Chenab_16	−2.25	0.04	−2.17	0.08	+0.20	0.10	+0.37	0.12	+0.37	0.07	+0.27	0.06	+0.21	0.07	+0.07	0.06	+0.06	0.17	+0.44	0.16	+0.44	0.08
Elqui_0	−2.42	0.06	−2.08	0.09	−0.52	0.17	−0.20	0.29	+0.27	0.12	+0.19	0.09	−0.14	0.13	−0.04	0.12	−0.20	0.17	−0.69	0.14	−0.07	0.09
Elqui_1	−3.01	0.06	−2.91	0.09	+0.29	0.13	+0.70	0.24	+0.94	0.11	+0.25	0.07	+0.06	0.10	+0.16	0.09	−0.10	0.26	−1.27	0.11	+0.17	lim
Elqui_3	−2.06	0.09	−1.81	0.09	+0.09	0.20	+0.20	0.15	−0.09	0.16	+0.17	0.10	−0.08	0.15	−0.16	0.12	+0.59	lim	+0.55	0.18	+0.20	0.13
Elqui_4	−2.27	0.05	−2.05	0.08	−0.53	0.12	−0.14	0.15	+0.01	0.08	+0.01	0.07	−0.11	0.10	−0.01	0.08	−0.59	0.21	−1.40	0.15	−0.17	lim
Indus_0	−2.46	0.05	−2.44	0.09	+0.20	0.09	+0.94	0.08	+0.40	0.07	+0.40	0.07	+0.24	0.08	+0.14	0.08	+0.25	0.19	+0.15	0.14	+0.42	0.09
Indus_12	−2.21	0.06	−2.13	0.10	−0.12	0.12	+0.20	0.13	+0.44	0.07	+0.34	0.07	+0.23	0.08	+0.07	0.08	−0.13	0.17	+0.05	0.16	+0.56	0.09
Indus_13	−2.04	0.07	−1.92	0.09	+0.19	0.14	+0.21	0.09	+0.30	0.08	+0.43	0.08	+0.33	0.09	+0.17	0.08	+0.71	0.09	+1.18	0.14	+1.77	0.08
Indus_14	−2.07	0.08	−1.98	0.10	+0.22	0.14	+0.13	0.09	+0.43	0.10	+0.39	0.10	+0.22	0.10	+0.10	0.10	+0.04	0.13	+0.17	0.16	+0.67	0.09
Indus_15	−1.77	0.05	−1.69	0.07	+0.19	0.13	+0.07	0.05	+0.45	0.08	+0.48	0.06	+0.29	0.09	−0.00	0.08	+0.31	0.10	+0.28	0.12	+0.40	0.06
Indus_6	−2.32	0.05	−2.35	0.10	+0.36	0.10	+0.33	0.16	+0.42	0.09	+0.47	0.08	+0.33	0.10	+0.06	0.12	−0.03	0.31	+0.06	0.13	+0.62	0.11
Indus_8	−2.04	0.05	−2.02	0.10	+0.24	0.12	+0.29	0.10	+0.33	0.08	+0.47	0.08	+0.24	0.10	+0.12	0.09	+0.02	0.19	−0.01	0.13	+0.44	0.11
Jhelum_0	−2.13	0.06	−2.04	0.08	+0.40	0.12	+0.40	0.08	+0.44	0.10	+0.33	0.08	+0.28	0.10	+0.28	0.10	+0.29	0.11	−0.02	0.13	+0.32	0.08
Jhelum_1_5	−2.17	0.06	−2.13	0.07	+0.30	0.10	+0.23	0.08	+0.40	0.08	+0.42	0.07	+0.34	0.09	+0.05	0.10	+0.15	0.12	+0.02	0.14	+0.51	0.07
Jhelum_1_8	−2.42	0.07	−2.42	0.11	+0.31	0.12	+0.27	0.10	+0.34	0.09	+0.28	0.08	+0.37	0.10	+0.00	0.09	+0.25	0.14	−0.12	0.13	+0.82	lim
Jhelum_2_10	−2.12	0.07	−2.03	0.08	+0.32	0.13	+0.27	0.08	+0.48	0.08	+0.47	0.07	+0.25	0.10	+0.15	0.09	+0.26	0.11	+0.21	0.15	+0.65	0.08
Jhelum_2_11	−2.21	0.06	−2.19	0.10	+0.39	0.10	+0.31	0.11	+0.43	0.09	+0.44	0.07	+0.50	0.09	−0.04	0.08	+0.27	0.15	−0.03	0.14	+0.53	0.09
Jhelum_2_14	−2.37	0.05	−2.39	0.09	+0.30	0.09	+0.09	0.17	+0.13	0.08	+0.15	0.08	+0.17	0.12	+0.06	0.10	−0.19	0.23	−0.91	0.13	+0.64	lim
Jhelum_2_15	−2.23	0.05	−2.13	0.09	+0.33	0.10	+0.35	0.10	+0.45	0.08	+0.43	0.07	+0.25	0.09	+0.12	0.08	+0.03	0.17	+0.02	0.14	+0.52	0.09
Jhelum_2_2	−1.67	0.08	−1.62	0.10	+0.12	0.15	−0.06	0.15	+0.35	0.10	+0.33	0.10	+0.17	0.10	−0.08	0.10	+0.22	0.09	+0.18	0.18	+0.46	0.08
Phoenix_1	−2.60	0.04	−2.52	0.16	+0.34	0.18	+0.29	0.12	+0.37	0.06	+0.29	0.05	+0.27	0.07	+0.04	0.09	+0.16	0.22	−1.06	0.14	+0.57	lim
Phoenix_10	−2.85	0.06	−2.93	0.09	+0.34	0.10	+0.57	0.22	+0.28	0.10	+0.20	0.08	+0.38	0.10	−0.10	0.23	−0.33	0.34	−0.67	0.17	+1.01	lim
Phoenix_2	−2.65	0.12	−2.62	0.10	+0.30	0.14	−0.20	0.18	+0.29	0.19	+0.44	0.18	⋯	⋯	+1.59	lim	−0.93	0.31	−1.20	0.27	+1.07	lim
Phoenix_3	−2.74	0.07	−2.70	0.12	+0.40	0.11	+0.27	0.21	+0.37	0.10	+0.13	0.09	+0.13	0.13	−0.07	0.26	−0.30	0.32	−0.91	0.19	+0.91	lim
Phoenix_6	−2.79	0.07	−2.68	0.15	+0.00	0.14	+0.15	0.30	+0.45	0.10	+0.09	0.10	+0.24	0.16	−0.34	0.32	−0.33	0.52	−0.89	0.19	+0.71	lim
Phoenix_7	−2.80	0.07	−2.62	0.08	+0.41	0.10	+0.61	0.10	+0.57	0.07	+0.37	0.07	+0.44	0.08	+0.28	0.12	+0.24	0.16	−1.04	0.12	+0.30	lim
Phoenix_8	−2.72	0.08	−2.79	0.09	+0.41	0.10	+0.34	0.07	+0.33	0.07	+0.23	0.08	+0.31	0.07	+0.17	0.09	−0.52	0.17	−0.99	0.24	+1.02	lim
Phoenix_9	−2.85	0.07	−2.71	0.08	+0.55	0.10	+0.03	0.18	+0.48	0.10	+0.40	0.08	+0.32	0.12	+0.02	0.25	−0.42	0.29	−1.08	0.25	+0.89	lim

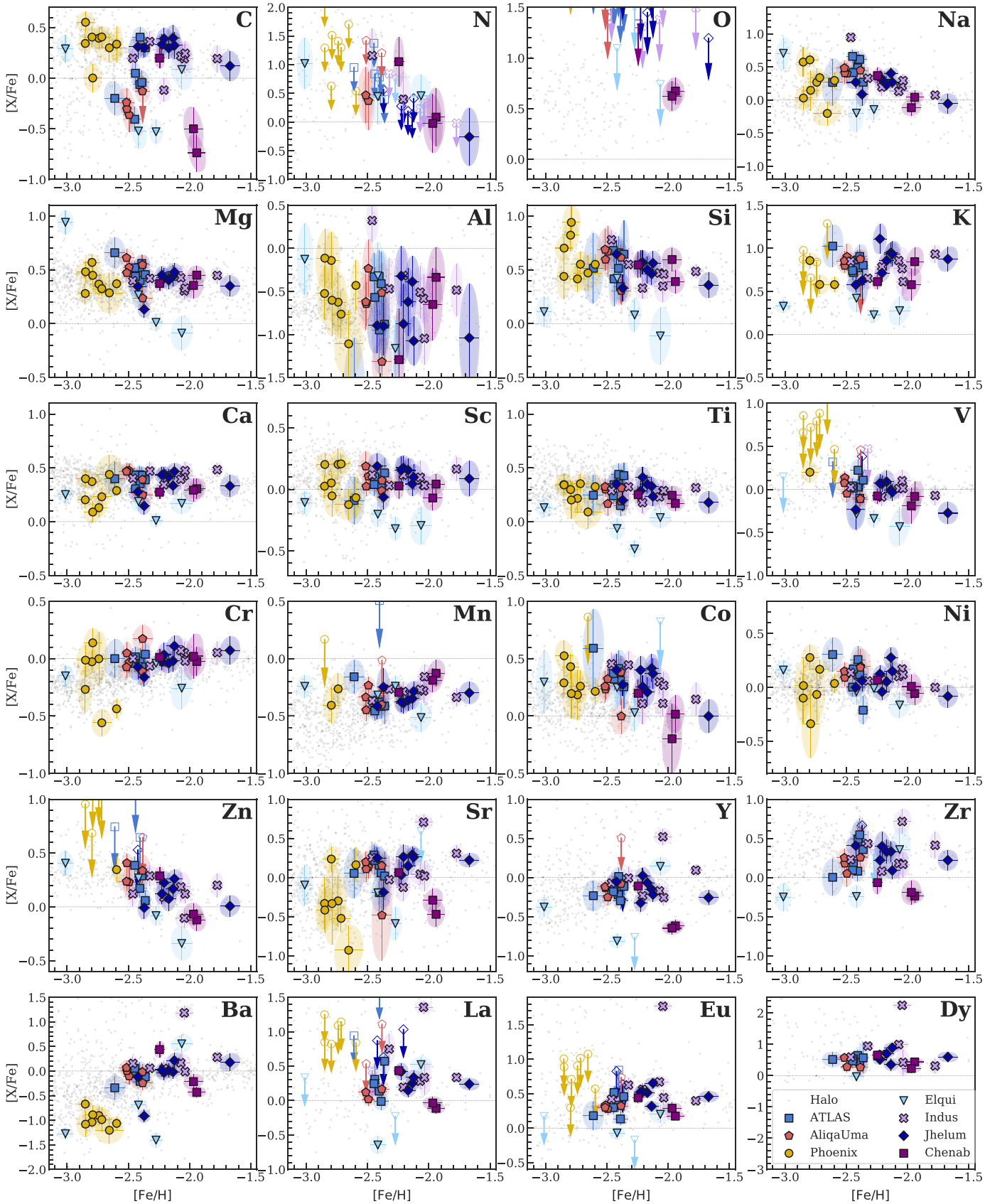

Figure 3. The [X/Fe] vs. [Fe I/H] for most elements measured in this paper. Here Cu, Ce, Nd, Sm, and Gd have not been included. Filled colored points indicate measurements, where the error ellipse represents the correlated [X/Fe] vs. [Fe I/H] errors after propagating stellar parameter uncertainties. Open symbols with downward-pointing arrows indicate upper limits. Gray points in the background are halo stars from JINAbase (Abohalima & Frebel 2018).

ratios where Fe can be either Fe I or Fe II. We use the species Ti II, V I, Cr I, and Sr II for those elements and C–H and C–N for the C and N abundances. We have not plotted Cu, Ce, Nd, Sm, and Gd. The error ellipses are the proper covariances between [X/Fe] and [Fe I/H], where any correlation is introduced solely through stellar parameters.

Individual correlations with stellar parameters are shown in Appendix D. The salient features of these figures will be discussed in Section 6. In brief summary, the elements C, N, Al, Sc, V, Mn, Co, Cu, Sr, Y, Zr, Ba, La, Eu, and Dy were measured with spectral synthesis, while the other elements, O, Na, Mg, Si, K, Ca, Ti, Cr, Fe, Ni, Zn, Ce, Nd, Sm, and Gd, were measured with equivalent widths. Species having known significant non-local thermodynamic equilibrium (NLTE) effects potentially in excess of 0.2 dex include Na I, Al I, K I, Ti I, Cr I, Mn I, and Fe I. The NLTE effects have not been included in this analysis.

6. Comments on Specific Elements

This section contains comments useful for interpreting the abundances of these elements, such as how the abundances were derived, and relevant caveats, such as sensitivity to stellar parameters or NLTE effects.

6.1. Carbon, Nitrogen, Oxygen

Carbon is measured from spectral synthesis of the CH molecular features at 4313 and 4323 Å, where each of these regions is treated independently. AliqaUma_0 has too low an S/N to measure a C abundance, so upper limits were placed. Here [C/Fe] clearly decreases as log g decreases, which is expected for red giants as they ascend the giant branch (e.g., Placco et al. 2014).

Oxygen affects the C abundance through CO molecular equilibrium, but we have only measured it in two stars. Thus, [O/Fe] = +0.4 was assumed throughout. Reducing to [O/Fe] = 0.0 decreases the [C/Fe] abundance by less than 0.05 dex for all of our stars, which we regard as negligible. Increasing to [O/Fe] = 1.0 increases [C/Fe] by less than 0.1 dex for most stars. We thus add an extra uncertainty of 0.1 dex in quadrature to the statistical [C/Fe] error (e_i in Table 5). This is mostly sufficient, but three of the coolest and most metal-rich stars ($T_{\rm eff} \lesssim 4300$ K, [Fe/H] $\gtrsim -1.9$) have much larger [C/Fe] differences when changing [O/Fe]: Chenab_12, Elqui_0, and Elqui_3 have [C/Fe] increase by 0.32, 0.18, and 0.29 dex, respectively, when increasing [O/Fe] to +1. For consistency, the systematic error was kept at 0.1 dex for these three stars.

For isotopes, the ratio $^{12}C/^{13}C = 9$ is assumed throughout. This value is chosen because all analyzed stars are RGB stars and have been through the first dredge-up that produces an equilibrium value of $^{12}C/^{13}C$ close to 9. Visually comparing synthetic spectra with different isotope ratios around 4224 and 4323 Å shows that this is a good assumption. In many cases, a typical higher value of $^{12}C/^{13}C = 99$ might provide a moderately better fit, and the stars Chenab_16 and Elqui_1 might have a $^{12}C/^{13}C$ as low as 4. However, the data generally do not have enough S/N to place a meaningful constraint on the isotope ratio.

When possible, N is measured by synthesizing the CN bands at 3865–3885 Å. This is done after measuring C from the CH bands. These bands are often detected in the cooler stars ($T_{\rm eff} < 4800$ K). Where not detected, an upper limit is synthesized, reported in Table 5. However, as mentioned in Section 4, upper limits for molecular features are likely underestimated because they do not include continuum placement uncertainty. The CN has some dependence on the C abundance, and due to this and the overall low S/N in the CN band region, we have applied a minimum 0.3 dex floor to the CN abundance uncertainty.

Two cool and relatively metal-rich stars in Chenab have O measured from equivalent widths of the forbidden lines at 6300 and 6363 Å. The two line abundances agree, but they are near telluric regions and affected by several systematic blends (Asplund et al. 2004), so they should be regarded with caution. For the other stars, O upper limits are found using the 6300 Å line.

6.2. Magnesium, Silicon, Calcium, Titanium

Magnesium is measured with equivalent widths of up to nine lines, with four lines detected in all stars (4702, 5172, 5183, and 5528 Å). The Mg b lines are often saturated and require fitting Voigt profiles to get an accurate equivalent width. After using Voigt profiles, their abundances agree with the other lines. The 4702 Å line tends to have the largest weight and thus the most influence on the final abundance. Note that there is a moderate anticorrelation between [Mg/Fe] and log g.

Silicon is the least reliable α-element measured. Across our sample, the 3905 and 4102 Å Si lines are always detected. Neither line provides a very reliable abundance, since the 3905 Å line is both saturated and blended, while the 4102 Å line is in the wing of a Balmer line. However, the resulting Si abundances tend to be reasonably close, though the 3905 Å line is biased lower. In stars with [Fe/H] $\gtrsim -1.9$, Si can be detected with lines from 5690 to 6000 Å. The 3905 Å line is synthesized due to a carbon blend, with equivalent widths used for the others.

Here Ca I is measured using equivalent widths of 25 lines. We specifically updated the Ca log gf values in `linemake` using VALD, because the original log gf values in `linemake` resulted in large Ca abundance scatter in standard stars. The number of measured Ca lines per star varies from 4 to 23, but restricting to the most common Ca lines (used in at least 30 of our 42 stars) makes a negligible -0.02 ± 0.03 dex difference. We consider Ca to be the most reliably measured α-element.

Titanium is usually considered as an α-element, although nucleosynthetically, it may be closer to Fe-peak elements like Sc and V (Cowan et al. 2020). Both Ti I and Ti II lines are measured using equivalent widths. The Ti II abundances are 0.09 ± 0.13 dex higher than the Ti I abundances. In metal-poor giants, Ti II abundances are more trustworthy than Ti I. There are more and stronger lines, and Ti I may be significantly affected by NLTE. Fifty-two unique Ti I lines were measured, of which only six are present in more than 30 stars of our sample. If we were to derive Ti I abundances using only these six lines, the abundances would change by -0.03 ± 0.11 dex, where the 0.11 dex scatter suggests that line selection can significantly affect a star's Ti I abundance (though not on average). For Ti II, 17 out of 65 lines are measured in more than 30 stars of our sample. Using just these lines results in abundances that change by only 0.04 ± 0.06 dex, further indicating that the Ti II abundances are more reliable.

6.3. Sodium, Aluminum, Potassium, Scandium

For cool and metal-poor giants, Na is almost always measured only from equivalent widths of two Na D resonance lines. The exception is the star AliqaUma_0, which has strong

sky-line residuals preventing a measurement or useful upper limit. The Na D lines often have slight negative NLTE corrections of −0.1 to −0.4 dex for cool and metal-poor stars that have not been applied here (Lind et al. 2011). The weaker Na lines at 5682 and 5688 Å are also detected in the cooler and more metal-rich stars ([Fe/H] > −2), where they agree with the Na D lines within 0.1 dex.

The only detectable Al lines in our spectra are the 3944 and 3961 Å lines, which are measured using spectral synthesis. It is unfortunately difficult to derive a reliable abundance from either line. Both lines are in the blue, where the S/N is lower; near strong hydrogen lines that affect continuum placement; and heavily affected by NLTE corrections of ∼+0.7 dex (Nordlander & Lind 2017). Furthermore, the 3944 Å line is heavily blended. We have added an extra 0.3 dex minimum systematic uncertainty to each Al line to account for the significant continuum modeling issues. Still, we encourage strong caution in using any of our Al abundances, as the abundance uncertainties are large and may still be underestimated.

Potassium is measured from the equivalent widths of the resonant K lines at 7665 and 7699 Å. The 7665 Å line is often blended with telluric absorption, in which case, that line is not used. In one star (ATLAS_22), the 7665 Å line is clean, but the 7699 Å line has a clear telluric blend. When the 7699 Å line is not detected, an upper limit is synthesized. There are moderate negative NLTE corrections for K that range from −0.0 to −0.4 dex (Reggiani et al. 2019).

Five bluer Sc II lines from 4246 to 4415 Å are detected in essentially all of our stars, while three redder lines are detected in most stars. These lines have hyperfine structure, and the bluest lines are often quite blended with carbon, so all Sc lines are synthesized. An extra 0.1 dex minimum systematic uncertainty per Sc line is added, because the hyperfine structure causes these line abundances to be sensitive to the synthesis smoothing kernel. The two bluest lines tend to have much lower weight than the other lines.

6.4. Vanadium, Chromium, Manganese

Two V I lines and two V II lines are measured using spectral syntheses due to hyperfine structure and strong or minor blends for all of the V lines under consideration. The V I 4379 Å line is the best line, though it has a minor blend with ^{12}CH. The V I 4384 Å line is often detected but heavily blended with an Sc and Fe line. The V II 4005 Å line is adjacent to and slightly blended with some strong Fe lines. The V II 3952 Å line is not usually measured because the S/N is lower and it is hard to determine the continuum in this region, but we report it when possible. Note that our error estimation does not propagate abundance uncertainties in the blending features, so the errors are likely underestimated for V. When both V I and V II are measured in a star, the V II abundances are 0.30 ± 0.23 dex higher than the V I abundances. This is larger than the individual V I or V II error, but it is similar to the [V II/V I] ratio found in Roederer et al. (2014). Because the V I lines are stronger in our stars, we use this is as the default V abundance in this paper's figures.

Equivalent widths of 17 Cr I lines in 41 stars and six Cr II lines in 33 stars are measured. The Cr II abundances are larger than Cr I by 0.18 ± 0.24 dex. Because Cr I is affected by NLTE (Bergemann & Cescutti 2010), the Cr II abundances should have fewer systematic errors, although the lines are noisier and detected less often. However, because Cr II is not detected in all of our stars, we default to the Cr I abundance in this paper's figures.

Up to six different Mn I lines are synthesized, at least one of which is detected in 35 of our stars. The resonant Mn triplet at 4030 Å is seen in all of our stars, but we never use these lines. The Mn is significantly affected by NLTE (Bergemann et al. 2019), and it is likely that the Mn triplet has a significantly different LTE-to-NLTE zero-point than the other lines. Even ignoring the Mn triplet, it is likely that the Mn abundances have a +0.4 to +0.6 dex correction. Like Sc, an extra 0.1 dex minimum systematic uncertainty is added per Mn line because the hyperfine structure causes these lines to be sensitive to the synthesis smoothing kernel.

6.5. Iron

Equivalent widths of plenty of Fe I and Fe II lines are measured in all of our stars, considering 175 Fe I lines and 30 Fe II lines. Typically, 100 Fe I lines are measured in each star, although there may be as few as 29 and as many as 130. The median number of Fe II lines is 18, with at least eight Fe II lines measured in all stars. The Fe II lines have been used to determine the microturbulence and model atmosphere metallicities of our stars.

We did not explicitly balance ionization states, and the Fe I and Fe II abundances thus usually differ by 0.08 dex with 0.11 dex scatter. Four stars have [Fe I/H] over 0.2 dex lower than [Fe II/H]: ATLAS_12 (0.29 dex), Elqui_0 (0.34 dex), Elqui_3 (0.25 dex), and Elqui_4 (0.22 dex). Such a difference is expected for the Elqui stars, as they are the coolest stars, and thus significant NLTE corrections apply (Bergemann et al. 2012; Mashonkina et al. 2016; Ezzeddine et al. 2017). The ATLAS_12 star had only seven Fe II lines, resulting in an unusually large microturbulence error that lowers the Fe I abundances but also substantially increases the [Fe I/H] error bar.

6.6. Cobalt, Nickel, Copper, Zinc

Four lines of Co at 4020, 4110, 4118, and 4121 Å are considered. These are synthesized to account for hyperfine structure. The Co lines often disagree substantially with each other, suggesting a possibly unaccounted-for systematic in their abundances or the line lists. The source of this discrepancy is not clear, but the quoted abundance errors reflect this disagreement by adding per-line systematic uncertainties to match the line-to-line scatter (Section 4.5, Appendix B).

The Ni I abundance is measured from equivalent widths. Up to 24 lines are measured in any individual star, though only two to four lines are detected in most stars. The strongest 5476 Å line is always detected or used to set an upper limit, with the next strongest lines at 4714, 6643, and 6767 Å.

One Cu I line at 5105 Å is detected in three of our most Fe-rich stars and measured using equivalent widths. A Cu upper limit is synthesized for the other stars.

Two Zn I lines are measured at 4810 and 4722 Å using equivalent widths. When both are present, they agree well, and sometimes only the 4810 Å line is present. We synthesize an upper limit with the 4810 Å line when neither is detected.

6.7. Strontium, Yttrium, Zirconium

The Sr II lines at 4077 and 4215 Å are detected in all but one of our stars. The exception is Elqui_3, a cool and metal-rich star with enough molecular absorption that these Sr lines

cannot be measured reliably. However, in this star and two other stars, the Sr I line at 4607 Å is detected. When both are measured, the Sr I line has a lower abundance by 0.15–0.30 dex than Sr II. The Sr II lines are measured using spectral synthesis, while the Sr I line is from an equivalent width. The Sr II lines are generally saturated, so they are strongly affected by microturbulence. As a result, Y and Zr are better tracers of a similar nucleosynthetic process when they are detected, although Sr provides good dynamic range.

A synthesis measurement or upper limit for Y II is found by examining three Y II lines in all of our stars (4398, 4883, and 4900 Å). If these are clearly detected, up to five other Y lines are measured. No Y lines are detected in the metal-poor Phoenix stream, and we do not place upper limits, as the Sr abundance is too low to expect a useful Y measurement or limit.

Only a single Zr II line at 4208 Å is measured, either synthesizing or placing an upper limit. Similar to Y, Zr is not considered in the Phoenix stream, as the limit is not meaningful.

6.8. Barium, Lanthanum

There are five strong lines for Ba II. The 4554 Å line is detected in every one of our stars, and the 4934 Å line is detected in all but a few Phoenix stars. The other three redder lines are weaker but generally detected in all but the Phoenix stars. The presence of hyperfine structure and isotopic splitting means that all Ba lines must be synthesized.

The isotope ratio (or, specifically, the even-to-odd isotope ratio $f_{\rm odd}$) can significantly impact the abundance derived from the two strongest Ba lines. In general, the detailed results require full 3D and NLTE modeling, as well as much higher S/N and resolution than achieved here (Gallagher et al. 2015). Thus, for simplicity, *r*-process isotope ratios were assumed for all of our stars (Sneden et al. 2008). If the solar Ba isotope ratios were used instead, the Ba abundance from the 4554 Å line would increase by up to 0.25 dex (Mashonkina & Belyaev 2019). Note that when the weaker Ba lines are detected, the abundance difference using just those lines is only 0.06 ± 0.09 dex higher compared to using all five lines. To account for the possible effect of isotope ratios, we have decided to add an extra uncertainty of 0.20 dex in quadrature to the error of the two strongest Ba lines. Because the abundance is somewhat dependent on the smoothing kernel, we have added an additional 0.1 dex systematic uncertainty to all Ba lines.

The production of La II is highly correlated with Ba, and, when detected, it is better than Ba because it is less saturated and not affected by isotopic ratios (Simmerer et al. 2004). Lanthanum has hyperfine splitting, so is measured with spectral synthesis. It is detected in about half our stars, and up to six La lines are considered, with the strongest one at 4086 Å. Since Ba is detected in all of our stars, an La limit is placed using the 4086 Å line in all of the stars, though it is often a very weak limit.

6.9. Europium, Dysprosium

The elements Eu and Dy primarily trace the *r*-process. In the solar system, over 98% of Eu and 88% of Dy comes from the *r*-process (e.g., Sneden et al. 2008).

Up to five lines of Eu II are synthesized at 4129, 4205, 4435, 4523, and 6645 Å. Usually, only the two bluest lines are detected and sufficiently strong to be used. Hyperfine structure and isotope splitting are included assuming the Sneden et al. (2008) isotope ratios.

One of the most abundant *r*-process elements is Dy II (e.g., Sneden et al. 2008), and two particularly strong lines are considered, one near the Sr 4077 Å line and one in the red wing of the 4102 Å Balmer line. Both of these lines are synthesized. We do not put upper limits on the Dy abundance, since when it is not detected, the Eu abundance is a more useful constraint on the *r*-process abundance of a star.

6.10. Other Neutron-capture Elements

Indus_13 is an *r*-process–enhanced star, and the continuum is substantially affected by the *r*-process elements. Thus, Ce, Nd, Sm, and Gd were also measured for this star. Many of these elements make a substantial impact on the overall continuum, which is the main reason these elements were measured. T. T. Hansen et al. (2020, in preparation) will present a more detailed analysis of this star.

Note that when considering all stars in all of our streams, many neutron-capture elements (Y, Zr, La, Eu, Dy) appear to have significant trends with the stellar parameters (see Appendix D). This is not a systematic effect but rather reflects the fact that each stream has intrinsically different neutron-capture element abundances, and due to their differing distances, they span a different range of stellar parameters. It just so happens that in this sample, stars in the furthest streams (i.e., coolest, lowest gravity, highest microturbulence stars) have lower overall neutron-capture element abundances than stars in closer streams.

7. Discussion

We first consider the metallicity distributions of the seven streams from high-resolution spectroscopy, providing some evidence for separating them into three thin globular cluster streams (ATLAS, Aliqa Uma, and Phoenix) and four thick dwarf galaxy streams (Chenab, Elqui, Indus, and Jhelum). We then briefly discuss each stream's abundances individually in the context of literature abundances of GCs and dwarf spheroidal (dSph) galaxies.

7.1. Stream Progenitors from Metallicity Spread

Shipp et al. (2018) classified the progenitors of the seven streams considered here as either GCs or dwarf galaxies. The classification was based on a mass-to-light ratio estimate, where the dynamical mass was inferred from the stream width and the luminous mass was inferred using isochrone models of the observed color–magnitude diagrams. These classifications can be refined by examining the metallicity dispersions. GCs display spreads of Fe-peak elements at a level of $\sim$0.03 dex (e.g., Gratton et al. 2004; Yong et al. 2013), which will be undetectable at our precision. Dwarf galaxies display significant [Fe/H] spreads in excess of 0.2 dex (e.g., Tolstoy et al. 2009; Leaman 2012; Willman & Strader 2012; Simon 2019).

Here we investigate the mean metallicity $\langle$[Fe/H]$\rangle$ and metallicity dispersion $\sigma_{\rm Fe}$ of these streams using the metallicities from high-resolution spectroscopy. Compared to the metallicities from AAT medium-resolution spectroscopy (Li et al. 2019), the high-resolution abundances are moderately more precise and likely more accurate. However, the sample sizes are smaller, with three to eight stars per stream. For the thick streams (Chenab, Elqui, Indus, and Jhelum), our target selection could have missed metal-rich member stars that are

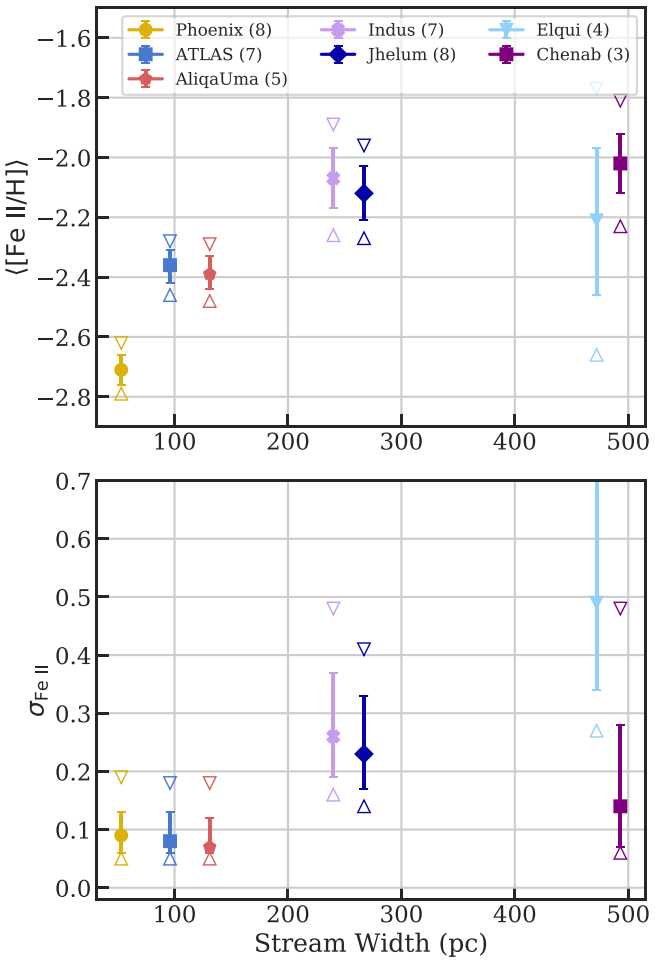

Figure 4. Mean metallicity (top panel) and metallicity dispersion (bottom panel) for high-resolution abundances in seven streams, plotted against the stream width (Shipp et al. 2018). The filled colored point indicates the median of the posterior samples, the error bars indicate the middle 68% scatter, and the open triangles indicate the 5th and 95th percentiles. The legend shows how many stars were analyzed in this paper for each stream. The three thinner streams have unresolved metallicity spreads, confirming their progenitors to be GCs.

harder to separate from the Milky Way foreground (see Sections 2 and 7.3). A detailed consideration of these effects will be discussed in subsequent work (A. Pace et al. 2020, in preparation).

The metallicity distribution of each stream was modeled as having an unknown mean abundance $\langle$[Fe/H]$\rangle$ and intrinsic scatter $\sigma_{\rm Fe}$. The Fe II abundance is used for [Fe/H], which is slightly less precise than Fe I due to having fewer lines but negligibly affected by systematic NLTE effects (e.g., Ezzeddine et al. 2017). Each star's observed metallicity was assumed to be drawn from this Gaussian distribution, plus Gaussian observational noise from $\sigma_{\rm [X/H]}$ from Table 6. We used an improper uniform prior for $\langle$[Fe/H]$\rangle$ and a uniform prior on $\log \sigma_{\rm Fe} \sim \mathcal{U}(-3, 0)$. The Hamiltonian Monte Carlo sampler implemented in `Stan` (Carpenter et al. 2017) was used to draw posterior samples for the mean and scatter for each stream.

The results are shown in Figure 4. The y-axis shows percentiles of the posterior distributions for $\langle$[Fe/H]$\rangle$ and $\sigma_{\rm Fe}$. The 5th/95th, 16th/84th, and 50th percentiles are shown as open triangles, error bars, and a solid point, respectively. The x-axis plots the physical stream width derived in Shipp et al. (2018). The legend shows how many stars were observed with MIKE in each stream. The top panel shows the mean metallicities for the streams, which are all in the range $-3 <$ [Fe/H] < -2. The Phoenix stream's progenitor would have been the lowest-metallicity globular cluster known (Wan et al. 2020).

The bottom panel of Figure 4 shows that the three thin streams have unresolved metallicity dispersions, with a 95% upper limit of about 0.2 dex. In contrast, the thicker streams mostly have clearly resolved metallicity dispersion. The exception is Chenab, which has only three stars, but it is still clearly a dwarf galaxy stream due to its connection with the Orphan stream (Section 7.3). Note that Aliqa Uma was tentatively classified as a possible dwarf galaxy stream based on its mass-to-light ratio (Shipp et al. 2018), but it is clearly a globular cluster stream and, in fact, an extension of ATLAS (Li et al. 2020). The metallicity dispersions here confirm that thin streams tend to be GCs, while thick streams tend to be dwarf galaxies.

Note that the exact value of the metallicity dispersion upper limit in our three globular cluster streams has some dependence on the prior, particularly the lower limit on $\log \sigma_{\rm Fe}$. Increasing the prior's lower limit to 10^{-2} dex would cause the 95% upper limits for ATLAS, Aliqa Uma, and Phoenix to increase by about 0.1 dex. Decreasing the lower limit to 10^{-4} dex would decrease the upper limits by about 0.05 dex. The smallest detected metallicity dispersions in star clusters are about 0.02 dex (Yong et al. 2013; Krumholz et al. 2019), so the minimum prior value must be less than 0.02. We have thus chosen a minimum of 0.001 to allow the result to reach a near-zero dispersion without artificially concentrating the prior at zero dispersion.

7.2. Globular Cluster Streams

Three streams (ATLAS, Aliqa Uma, and Phoenix) have thin morphologies and small velocity and metallicity dispersions that suggest that they are disrupted GCs (Shipp et al. 2018; Li et al. 2019). GCs show light-element variations (C through Si) that vary in specific patterns due to the CNO, Ne–Na, and Mg–Al proton-capture cycles. In general, the abundances of ^{13}C, ^{14}N, ^{23}Na, ^{27}Al, and ^{28}Si increase, while the abundances of ^{12}C, ^{16}O, ^{20}Ne, and ^{24}Mg decrease (e.g., Gratton et al. 2012, 2019). In NGC 2419 and NGC 2808, some unknown process also induces an Mg–K anticorrelation (Cohen & Kirby 2012; see discussion in Kemp et al. 2018).

Figure 5 shows the relevant measurable elements for our globular cluster streams. Of these elements, C, Na, and Mg are the most reliably measured elements in our globular cluster streams. In a few stars, N can be measured from the CN bands; the rest have upper limits that should be treated with caution (Section 4.4). Si and K are only measured from one to two lines, but these should be reliable. However, Al is measured from the 3944 and 3961 Å lines, with a large NLTE correction that should be considered in any interpretation. For comparison, globular cluster abundances from Carreta et al. (2009a), C and N abundances in NGC 7078 from Roediger et al. (2014), and K and Mg abundances in NGC 2419 from Mucciarelli (2012) are plotted as colored crosses. We have only included the most metal-poor GCs with [Fe/H] < -1.9, matching our stream metallicities.

No clear evidence is seen for the expected globular cluster abundance trends for any elements in our stellar streams. The most significant trend is the Na–Mg anticorrelation, which may

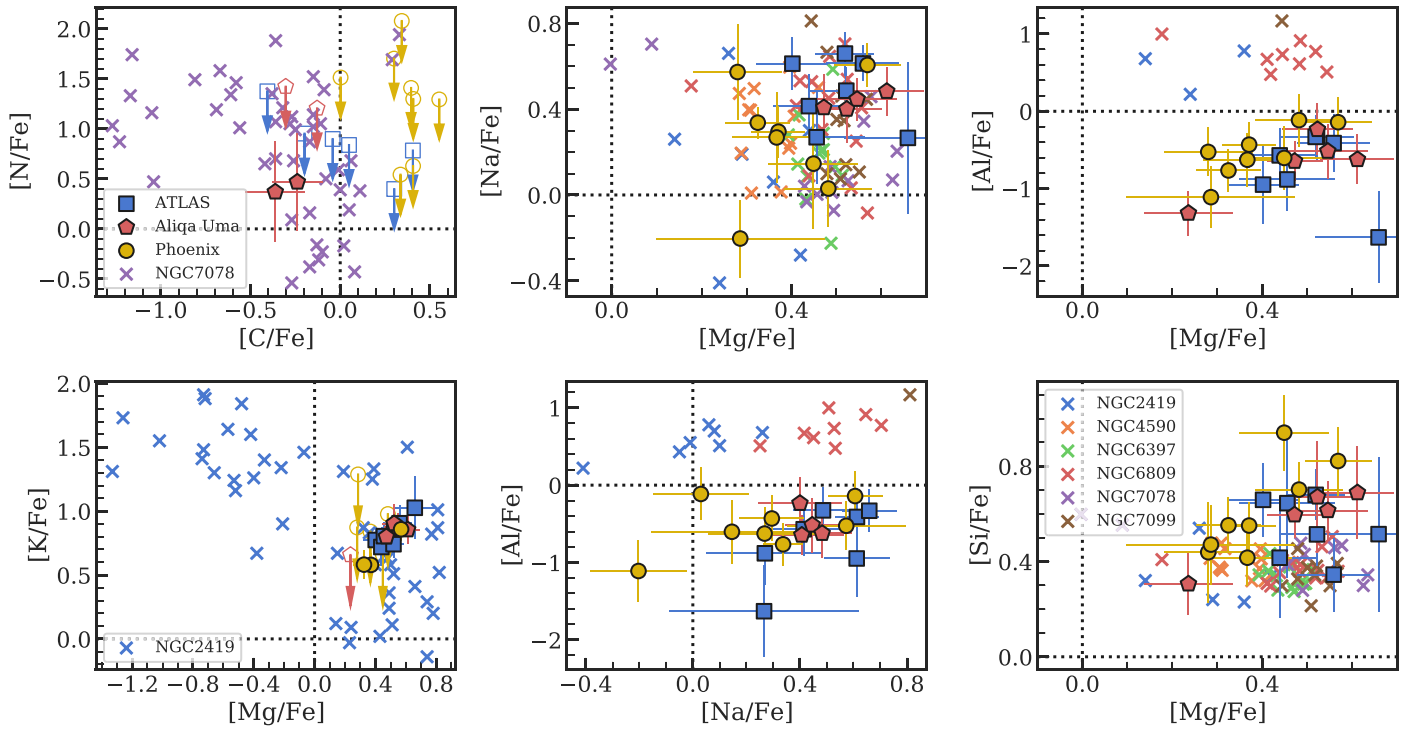

Figure 5. Globular cluster element trends compared to our measurements for globular cluster streams ATLAS, Aliqa Uma, and Phoenix. Crosses indicate literature abundances for GCs with [Fe/H] < -1.9 (Roediger et al. 2014 for top left C–N panel; Mucciarelli et al. 2012 for bottom left Mg–K panel; Carretta et al. 2009a for the rest), while open symbols with a downward-pointing arrow indicate upper limits in our streams (as in Figure 3). Note that the large zero-point offset in [Al/Fe] is due to NLTE effects (see Section 6).

be present in ATLAS and Phoenix but is consistent with noise. This is not especially surprising given the abundance uncertainties, the relatively small number of stars, and the fact that metal-poor GCs tend to have the least extreme abundance differences (Carretta et al. 2009b). In particular, due to the logarithmic nature of abundance measurements, we are only likely to detect the abundance increases for the odd-Z elements N, Na, and Al. This is because the proton-capture cycles convert abundant elements (O, Ne, Mg) to underabundant elements (N, Na, Al) while conserving the total heavy-element nuclei. In other words, since the cycle inputs O, Ne, and Mg are intrinsically $\gtrsim$10$\times$ more abundant than the cycle products N, Na, and Al, logarithmic increases in N, Na, and Al will be seen before significant logarithmic decreases in O, Ne, or Mg. More detailed quantification is reserved for future work (A. R. Casey et al. 2020, in preparation).

7.2.1. ATLAS and Aliqa Uma

These two streams are spatially and kinematically consistent with being a single stream whose progenitor is a globular cluster (Li et al. 2019, 2020). ATLAS and Aliqa Uma form a continuous track in radial velocity and proper motion on the sky, but, as discussed in Li et al. (2020), a massive perturber created a spatial kink that caused them to be initially classified as two separate streams in Shipp et al. (2018). The stellar abundances support this conclusion; both streams have essentially identical abundance character in all elements, with no detected metallicity spread and nearly identical abundance ratios (Li et al. 2020). There is weak evidence for larger scatter in the light elements Na and Mg, and they are anticorrelated in the direction that would be expected for a globular cluster. Like most GCs, all [X/Fe] ratios of the heavier elements are consistent with those seen in the stellar halo (e.g., Pritzl et al. 2005). Combining all of the stars in both streams gives a metallicity dispersion 95% confidence upper limit of 0.12 dex.

7.2.2. Phoenix

The progenitor of the thin Phoenix stream is likely a globular cluster. Its low inferred metallicity of [Fe/H] $= -2.7$ is below the globular cluster floor of -2.4, demonstrating that GCs below the metallicity floor previously existed, but they have probably mostly been tidally disrupted during Galactic evolution (Kruijssen 2019; Wan et al. 2020). The mean abundance ratios are mostly consistent with the stellar halo, with the exception being [Ba/Fe], which is significantly lower and suggests that Phoenix's progenitor was born in a lower-mass galaxy than most GCs. In addition, one star is clearly a lithium-rich giant. The abundances of this stream are discussed in detail by A. R. Casey et al. (2020, in preparation).

7.3. Dwarf Galaxy Streams

Four of our streams have thick morphologies, as well as significant metallicity dispersions and larger velocity dispersions that imply they are disrupting dwarf galaxies (Shipp et al. 2018; Li et al. 2019).

Figure 6 compares several relevant element abundances to literature dSph abundances spanning the full range of satellite galaxy luminosities: Sagittarius (Majewski et al. 2017; Hansen et al. 2018), Fornax (Shetrone et al. 2003; Letarte et al. 2010; Tafelmeyer et al. 2010), Sculptor (Shetrone et al. 2003; Geisler et al. 2005; Frebel et al. 2010; Kirby & Cohen 2012; Jablonka et al. 2015; Simon et al. 2015; Skúladóttir et al. 2015; Hill et al. 2019), Carina (Shetrone et al. 2003; Lemasle et al. 2012; Venn et al. 2012; Norris et al. 2017), Draco (Shetrone et al. 2001;

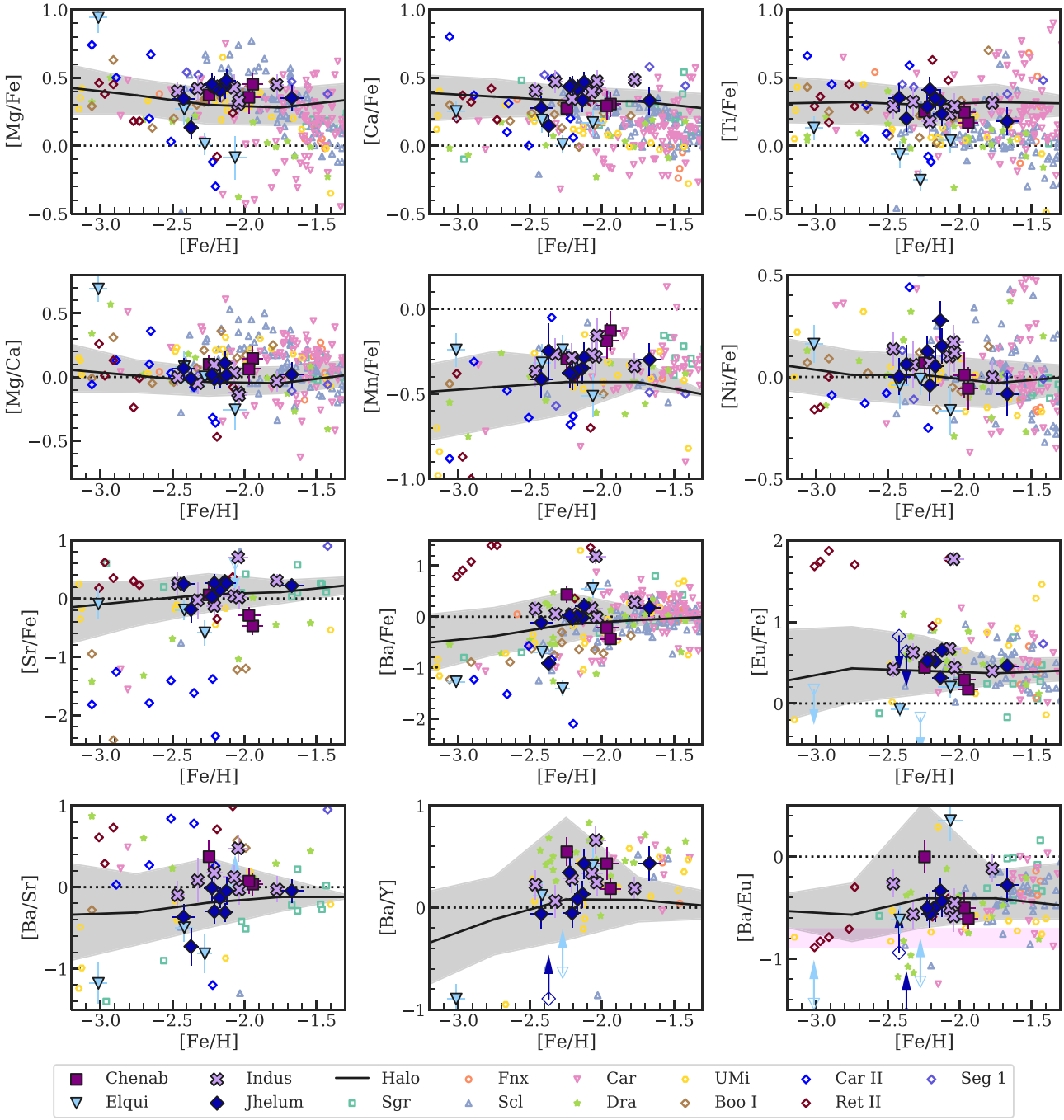

Figure 6. Abundance ratios of thick dSph streams (large filled points, upper limits with arrows) compared to dSph galaxies (small open points) and the halo median and 68% scatter (black line and shaded region). The shaded pink region in the [Ba/Eu] panel shows a pure *r*-process ratio.

Fulbright et al. 2004; Cohen & Huang 2009; Tsujimoto et al. 2015, 2017), Ursa Minor (Shetrone et al. 2001; Aoki et al. 2007; Cohen & Huang 2010; Kirby & Cohen 2012; Ural et al. 2015), Boötes I (Norris et al. 2010a, 2010b; Gilmore et al. 2013; Ishigaki et al. 2014; Frebel et al. 2016), Carina II (Ji et al. 2020), Reticulum II (Ji et al. 2016; Roederer et al. 2016), and Segue 1 (Frebel et al. 2014). For clarity, no upper limits are plotted for the literature sample.

Many of the Sgr stars come from APOGEE DR16 (Nidever et al. 2015; Shetrone et al. 2015; García Pérez et al. 2016; Majewski et al. 2017; Zasowski et al. 2017; Wilson et al. 2019; Jönsson et al. 2020). These are selected using the quality cuts STARFLAG = ASPCAPFLAG = 0, VERR $< 0.2\,\mathrm{km\,s^{-1}}$, S/N > 70, $T_{\rm eff} > 3700$ K, and $\log g < 3.5$ (Hayes et al. 2020). Only stars within 1.5 half-light radii of the Sgr center, or 514.″05 of $(\alpha, \delta) = (283.747, -30.4606)$ (Majewski et al. 2003), are considered. After inspection, Milky Way foreground stars are removed with velocity and proper-motion cuts of $100\,\mathrm{km\,s^{-1}} <$ VHELIO_AVG $< 180\,\mathrm{km\,s^{-1}}$, $-3.2\,\mathrm{mas\,yr^{-1}} <$ GAIA_PMRA $< -2.25\,\mathrm{mas\,yr^{-1}}$, and $-1.9\,\mathrm{mas\,yr^{-1}} <$ GAIA_PMDEC $< -0.9\,\mathrm{mas\,yr^{-1}}$. The final APOGEE selection has 400 stars.

Figure 6 also shows abundances in the Milky Way halo and disk collected in JINAbase (Abohalima & Frebel 2018) using only data from Fulbright (2000), Barklem et al. (2005), Aoki et al. (2009), Cohen et al. (2013), and Roederer et al. (2014).

For clarity, the halo stars are grouped in bins of 0.5 dex, plotting the median (black line) and 68% scatter (shaded gray region) of each bin.

The top row of Figure 6 shows [Mg, Ca, Ti/Fe] versus [Fe/H], which tracks the general star formation efficiency of a dwarf galaxy (e.g., Tinsley 1980; Matteucci & Brocato 1990; Tolstoy et al. 2009; Kirby et al. 2011). The only stream showing significant declines in [α/Fe] is Elqui, while the other streams are generally consistent with the halo median. There is also significant evolution in [Mg/Ca] with [Fe/H] in Elqui, while the other streams generally match the flat halo trend.

Also shown are [Mn, Ni/Fe], which can track changes in Type Ia supernova enrichment (McWilliam et al. 2018; Kirby et al. 2019; de los Reyes et al. 2020). These elements do not display any large trends with [Fe/H], although there is a hint that Chenab's metal-rich stars have higher [Mn/Fe].

The bottom two rows show the neutron-capture elements. Shown are [Sr, Ba, Eu/Fe] as the most easily measured tracers of elements from the first, second, and rare-earth neutron-capture peaks. In terms of neutron-capture element abundances, the stream stars are very similar to the luminous dSph galaxies, but they differ from the ultra-faint dSphs. The dSphs differ from the halo primarily in Ba, which is substantially lower than the halo at [Fe/H] $\lesssim -2.2$. The bottom row shows [Ba/Sr] and [Ba/Y]. The high-Fe dSph stars have elevated [Ba/Y] ratios compared to the halo, which is often interpreted as evidence for a metal-poor *s*-process taking place in dwarf galaxies (e.g., Shetrone et al. 2003; Venn et al. 2004). Here [Ba/Eu] indicates the relative ratio of *s*- and *r*-process, where the shaded pink region is a pure *r*-process [Ba/Eu] and higher values indicate some amount of *s*-process contamination (e.g., Sneden et al. 2008).

7.3.1. Chenab

The Chenab stream is a southern hemisphere extension of the Orphan stream (Koposov et al. 2019). Using RR Lyrae star counts, the progenitor is estimated to have a luminosity $M_V = -10.8 \pm 1.3$, placing its mass as similar to Sculptor and between that of Sextans and Leo I (Muñoz et al. 2018; Koposov et al. 2019). This matches the expectations found through high-resolution spectroscopic study of three Orphan stream stars by Casey et al. (2014), and our three new stars confirm previous conclusions, especially in having high [Ba/Y] ratios characteristic of intact dwarf galaxies.

Unlike Casey et al. (2014) we do not find a decreasing [α/Fe] trend with metallicity, but our stars span a smaller [Fe/H] range and may still be on the [α/Fe] plateau, implying an [α/Fe] knee somewhere in the range $-2.0 <$ [Fe/H] < -1.5, consistent with Sculptor (Hill et al. 2019). There is some evidence in our data for an upturn in [Mn/Fe] for the two more Fe-rich stars, a trend that continues in the stars from Casey et al. (2014). This could indicate a transition from sub-Chandrasekhar to Chandrasekhar-mass Type Ia supernovae (de los Reyes et al. 2020), although there is no corresponding rise in [Ni/Fe] (Kirby et al. 2019).

7.3.2. Elqui

The Elqui stream's dwarf galaxy progenitor is likely the lowest-mass galaxy progenitor of the streams studied here. Morphologically, this was already suggested using the progenitor masses derived in Shipp et al. (2018). The four Elqui stars are in the range $-3 <$ [Fe/H] < -2, and the most metal-rich stars in Elqui have [α/Fe] ~ 0, distinctly lower than the other streams and the stellar halo at this metallicity but similar to that of low-mass galaxies like Draco. The neutron-capture elements in Elqui display solar [Sr/Fe] ~ 0, much higher than the Sr in most lower-mass ultra-faint dwarf galaxies. The exception is Reticulum II, which has very different [Ba/Fe] from Elqui. Together, these trends suggest that Elqui's progenitor galaxy's stellar mass was at the low end of classical dSph galaxies, around $10^6\ M_\odot$, or $M_V \sim -9$.

Elqui_3 has a clear *s*-process signature with moderately enhanced Ba and C and [Ba/Eu] > 0. It is not clear if this is due to binary mass transfer or interstellar medium enrichment; no velocity variations are found in this star, and the enhancements are not as extreme as the CEMP-s stars that are clearly the result of mass transfer (e.g., Hansen et al. 2016).

Elqui_1 is the most Fe-poor star in our sample at [Fe/H] ~ -3. This star is likely C-enhanced, as it has $T_{\rm eff} \sim 4300$ K but [C/Fe] ~ 0.3. The Placco et al. (2014) correction[29] for this star gives [C/Fe] $\sim +1.0$. This star also has a very high [Mg/Fe] ~ 1.0 but low [Si/Fe] ~ 0.1 and [Ca/Fe] ~ 0.2, possibly suggesting that it is a carbon-enhanced star primarily enriched by a very massive star. Indeed, the [Fe/H], [Mg/C], [N/Na], and [Sc/Mn] abundances all suggest that this star has a high chance of being enriched by only one Population III supernova, according to the models in Hartwig et al. (2018). Furthermore, Elqui displays a much more rapid decline in [Mg/Fe] versus [Fe/H] compared to [Ca/Fe] versus [Fe/H], reminiscent of a few other dwarf galaxies like Sgr and Carina II (McWilliam et al. 2013; Hasselquist et al. 2017; Ji et al. 2020).

7.3.3. Indus and Jhelum

We consider Indus and Jhelum together because it has been suggested that they are two wraps of the same stream (Shipp et al. 2018; Bonaca et al. 2019). Jhelum also may have two separate spatial and/or kinematic populations (Bonaca et al. 2019; Shipp et al. 2019). Differences in elemental abundances could help verify whether the kinematic and spatial populations are in fact different systems, but by eye, the stars in these two streams have very similar abundances to each other and the background stellar halo. A more detailed analysis will be presented in A. Pace et al. (2020, in preparation).

There is a mild discrepancy between the median metallicity of our Indus and Jhelum stars and the [α/Fe] ratios observed in those stars. Most of the observed stars in these two streams have [Fe/H] ~ -2. Intact dwarf galaxies with $\langle$[Fe/H]$\rangle \sim -2$ have luminosities $-10 \lesssim M_V \lesssim -8$ (Carina, Ursa Minor, Sextans, Draco, Canes Venatici I; from the compilation in Muñoz et al. 2018; Simon 2019). However, all of the stars in these two streams are α-enhanced, with [Mg, Ca, Ti/Fe] $\sim +0.3$ to $+0.4$. Only relatively luminous galaxies, $M_V \gtrsim -10$, have enhanced [α/Fe] at [Fe/H] ~ -2 (e.g., Kirby et al. 2011). The most likely explanation for this discrepancy is that the stars observed here are somewhat biased toward lower metallicity compared to all possible Indus and Jhelum members. A. Pace et al. (2020, in preparation) and T. T. Hansen et al. (2020, in preparation) will discuss this in more detail.

One star in Indus (Indus_13) has extremely high levels of *r*-process enhancement, with [Eu/Fe] $\sim +1.8$ and [Fe/H] ~ -2.0. This is one of the most Fe-rich *r*-process–enhanced stars known,

[29] http://vplacco.pythonanywhere.com/

though similar stars have been found in Ursa Minor and the stellar halo (Aoki et al. 2007; Sakari et al. 2018). Additionally, one star in Indus (Indus_0) has high N, Na, and Al, consistent with globular cluster abundance anomalies. Stars in dSphs showing these anomalies are rare, though the anomalies are known to occur in the GCs associated with the Fornax dSph (e.g., Larsen et al. 2014; Hendricks et al. 2016). T. T. Hansen et al. (2020, in preparation) will discuss these stars and their implications for the formation of Indus's progenitor.

8. Summary

We have presented results from high-resolution spectroscopy of 42 red giant stars in seven stellar streams, including abundances of up to 30 elements. Three streams are from disrupted GCs with [Fe/H] < -2 (ATLAS, Aliqa Uma, and Phoenix). Four streams (Chenab, Elqui, Indus, and Jhelum) are disrupted dwarf galaxies with chemical evolution histories suggesting progenitor masses between Draco and Sculptor ($M_\star \sim 10^{6-7}\ M_\odot$).

The primary aim of this work was to present the detailed abundance analysis methodology. The main results are shown in Figure 3. The stellar parameters were derived using photometric temperatures and surface gravities, while microturbulence was inferred from Fe II lines (Table 2). A 1D LTE abundance analysis was performed using `MOOG` and `ATLAS` model atmospheres, propagating individual line uncertainties (Table 5) and accounting for correlated stellar parameters (Tables 4 and 6; see Appendix B). We recommend that those using the abundances in this paper read through Section 6 to understand how the abundances were derived and consider the figures in Appendix D to see if those correlations affect interpretations.

Figure 4 shows the relation between stream widths and metallicity dispersions, showing a separation between the thin globular cluster streams with unresolved metallicity dispersions and the thicker dwarf galaxy streams with resolved metallicity dispersions. Figures 5 and 6 show our results compared to literature values for intact GCs and dwarf galaxies. This paper has made few scientific interpretations, and future work will discuss specific streams in detail.

We thank the referee for important and thorough comments regarding this long paper. A.P.J. and T.S.L. are supported by NASA through Hubble Fellowship grants HST-HF2-51393.001 and HST-HF2-51439.001, respectively, awarded by the Space Telescope Science Institute, which is operated by the Association of Universities for Research in Astronomy, Inc., for NASA, under contract NAS5-26555. A.P.J. is partially supported by the Thacher Research Award in Astronomy. A.R.C. is supported in part by the Australian Research Council through a Discovery Early Career Researcher Award (DE190100656). Parts of this research were supported by the Australian Research Council Centre of Excellence for All Sky Astrophysics in 3 Dimensions (ASTRO 3D) through project No. CE170100013. A.B.P. acknowledges support from NSF grant AST-1813881. S.K. is partially supported by NSF grants AST-1813881 and AST-1909584 and Heising-Simons foundation grant 2018-1030. S.L.M. and J.D.S. acknowledge support from the Australian Research Council through Discovery Project grant DP180101791.

This research has made use of the SIMBAD database, operated at CDS, Strasbourg, France (Wenger et al. 2000), and NASA's Astrophysics Data System Bibliographic Services. This work has made use of the VALD database, operated at Uppsala University, the Institute of Astronomy RAS in Moscow, and the University of Vienna. This work presents results from the European Space Agency (ESA) space mission Gaia. The Gaia data are being processed by the Gaia Data Processing and Analysis Consortium (DPAC). Funding for the DPAC is provided by national institutions, in particular the institutions participating in the Gaia MultiLateral Agreement (MLA). The Gaia mission website is https://www.cosmos.esa.int/gaia. The Gaia archive website is https://archives.esac.esa.int/gaia. This project used public archival data from the Dark Energy Survey (DES). Funding for the DES Projects has been provided by the U.S. Department of Energy, the U.S. National Science Foundation, the Ministry of Science and Education of Spain, the Science and Technology Facilities Council of the United Kingdom, the Higher Education Funding Council for England, the National Center for Supercomputing Applications at the University of Illinois at Urbana-Champaign, the Kavli Institute of Cosmological Physics at the University of Chicago, the Center for Cosmology and Astro-Particle Physics at the Ohio State University, the Mitchell Institute for Fundamental Physics and Astronomy at Texas A&M University, Financiadora de Estudos e Projetos, Fundação Carlos Chagas Filho de Amparo à Pesquisa do Estado do Rio de Janeiro, Conselho Nacional de Desenvolvimento Científico e Tecnológico and the Ministério da Ciência, Tecnologia e Inovação, the Deutsche Forschungsgemeinschaft, and the Collaborating Institutions in the Dark Energy Survey. The Collaborating Institutions are Argonne National Laboratory, the University of California at Santa Cruz, the University of Cambridge, Centro de Investigaciones Energéticas, Medioambientales y Tecnológicas-Madrid, the University of Chicago, University College London, the DES-Brazil Consortium, the University of Edinburgh, the Eidgenössische Technische Hochschule (ETH) Zürich, Fermi National Accelerator Laboratory, the University of Illinois at Urbana-Champaign, the Institut de Ciències de l'Espai (IEEC/CSIC), the Institut de Física d'Altes Energies, Lawrence Berkeley National Laboratory, the Ludwig-Maximilians Universität München and the associated Excellence Cluster Universe, the University of Michigan, the National Optical Astronomy Observatory, the University of Nottingham, The Ohio State University, the OzDES Membership Consortium, the University of Pennsylvania, the University of Portsmouth, SLAC National Accelerator Laboratory, Stanford University, the University of Sussex, and Texas A&M University. Based in part on observations at Cerro Tololo Inter-American Observatory, National Optical Astronomy Observatory, which is operated by the Association of Universities for Research in Astronomy (AURA) under a cooperative agreement with the National Science Foundation.

Facility: Anglo-Australian Telescope (AAOmega+2dF); Magellan/Clay (MIKE).

Software: `numpy` (van der Walt et al. 2011), `scipy` (Jones et al. 2001), `matplotlib` (Hunter 2007), `pandas` (McKinney 2010), `seaborn` (Waskom et al. 2016), `astropy` (Astropy Collaboration et al. 2013; Price-Whelan et al. 2018), `emcee` (Foreman-Mackey et al. 2013), `CarPy` (Kelson 2003), `MOOG` (Sneden 1973; Sobeck et al. 2011), `SMHR` (Casey 2014), `rvspecfit` (Koposov 2019), `PyStan` (Carpenter et al. 2017; Stan Development Team 2018).

Appendix A
Stellar Parameter Comparisons

A.1. Comparison to LTE Spectroscopic-only Parameters

A standard LTE stellar parameter analysis is done for comparison and verification. We determine $T_{\rm eff}$ by balancing Fe I abundance versus excitation potential, $\log g$ by balancing Fe I and Fe II abundances, and ν_t by balancing Fe II abundance versus reduced equivalent width, and we set [M/H] to the Fe II abundance. The LTE-only stellar parameters are compared to the fiducial parameters in Figure A1. Because of the NLTE effects of Fe I, such LTE analysis in cool, metal-poor stars like ours tends to produce cooler temperatures and lower $\log g$ compared to photometric temperatures and theoretical isochrones (e.g., Ezzeddine et al. 2017). A pure LTE analysis would thus also shift ν_t and [M/H] to higher and lower values, respectively. In our sample, the median offset and half-of-68% scatter is $\Delta T_{\rm eff} = -272 \pm 129$ K, $\Delta \log g = -0.55 \pm 0.32$ dex, $\Delta \nu_t = 0.04 \pm 0.08\,{\rm km\,s^{-1}}$, and Δ [M/H] $= -0.22 \pm 0.13$, where the sign of Δ is LTE − fiducial.

The LTE stellar parameters rely only on spectroscopy and show all stars to be red giants. This verifies that our stars are not foreground dwarf interlopers and justifies the use of photometric stellar parameters.

Note that the photometric and isochrone-based parameters suggest that a linear correction to an LTE-only $T_{\rm eff}$ (e.g., Frebel et al. 2013a) is insufficient to describe the transformation to a photometric $T_{\rm eff}$.

A.2. Comparison to `rvspecfit` Stellar Parameters

The AAT spectra used to identify these stream targets (Li et al. 2019) had stellar parameters and metallicities determined by `rvspecfit` (Koposov et al. 2011; Koposov 2019). This is a full-spectrum fit using the `PHOENIX-2.0` spectral grid (Husser et al. 2013). The comparison is shown in Figure A2. The left column shows the comparison to values determined from the red 1700D grating ($R \sim 10{,}000$, 8420–8820 Å), while the right shows values determined from the blue 580V grating ($R \sim 1300$, 3800–5800 Å).

In general, there are clear differences in the AAT stellar parameters compared to the MIKE stellar parameters. On the red side, the differences could be attributed to the fact that the AAT is effectively doing an LTE spectroscopic parameter determination. Comparing the left column of Figure A2 to Figure A1, the $T_{\rm eff}$ and $\log g$ trends are similar for the bulk of the stars, failing mostly on the coolest stars. On the blue side, `rvspecfit` prefers higher $T_{\rm eff}$, $\log g$, and [M/H] compared to the derived MIKE values. The origin of this difference is less

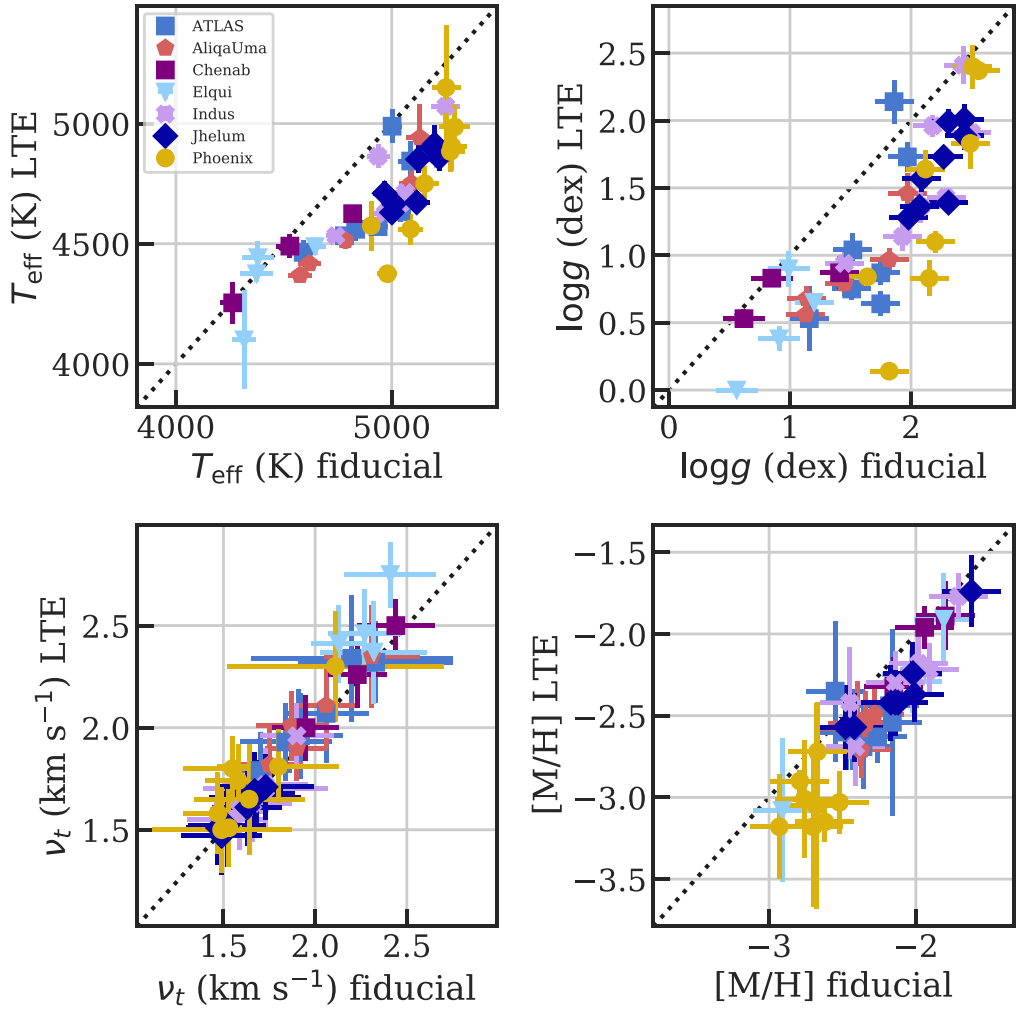

Figure A1. Comparison of the adopted fiducial stellar parameters to parameters from a standard 1D LTE analysis. See text for details.

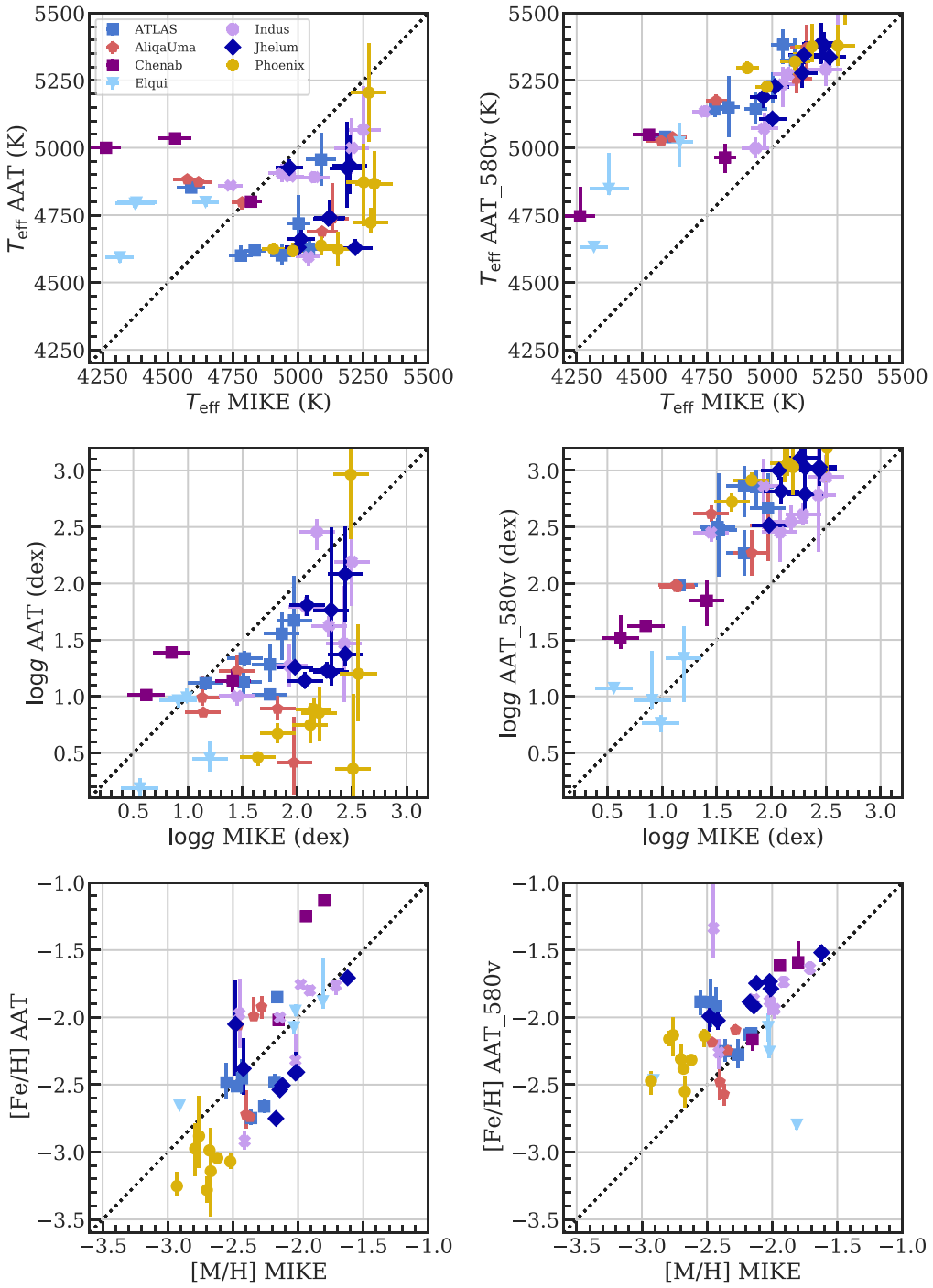

Figure A2. Comparison of MIKE to AAT stellar parameters. The left column is the fit to the Ca triplet (1700D grating, $R \sim 10{,}000$, 8420–8820 Å), and the right column is to the blue arm (580V grating, $R \sim 1300$, 3800–5800 Å).

clear but could be due to difficulties modeling Balmer line shapes biasing temperatures to be high. However, in both cases, the metallicities are reasonably consistent, especially the relative metallicities.

Appendix B
A New Framework for Abundance Means and Uncertainties

Here we describe and derive how to combine individual line measurements into final abundances and uncertainties. We consider individual line errors and responses to stellar parameters, self-consistently estimate and include systematic uncertainties, and fully propagate all stellar parameter correlations to both the mean and error of the final abundance. The propagation of stellar parameters to abundance errors is similar to that in the literature (e.g., McWilliam et al. 1995). However, previous treatments did not consider the effect of stellar parameter correlations on the abundance mean.

Consider a star with measured stellar parameters θ_k for $k = 1$–4 (i.e., $\theta_1 = T_{\rm eff}$, $\theta_2 = \log g$, $\theta_3 = \nu_t$, $\theta_4 = [{\rm M/H}]$). We assume θ is drawn from a multivariate normal distribution $\theta \sim \mathcal{N}(\Theta, \Sigma_\theta)$, where Θ is the true stellar parameters and Σ_θ is

the covariance matrix taken from combining the individual stellar parameter uncertainties σ_θ and the correlation matrix ρ_{kl}. Define $\delta\theta = \theta - \Theta$ to be the stellar parameter error, which has the distribution $\delta\theta \sim \mathcal{N}(0, \Sigma_\theta)$.

Consider a species X in this star that is measured by N lines indexed by $i = 1, \ldots N$. Each line has a measured abundance x_i, a statistical error e_i, and gradients with respect to each stellar parameter $G_{i,k} = \delta_{i,k}/\sigma_{\theta,k}$, where $\delta_{i,k}$ is defined as in Table 5. Our model for x_i is

$$\begin{aligned} x_i &= x_{\rm True} + \epsilon_i + \sum_k G_{i,k}\delta\theta_k \\ &= x_{\rm True} + \epsilon_i + G_i^T\,\delta\theta, \end{aligned} \tag{B1}$$

where $x_{\rm True}$ is the true abundance of species X, $\epsilon_i \sim \mathcal{N}(0, e_i^2)$ is the random offset from the true value, and $\delta\theta \sim \mathcal{N}(0, \Sigma_\theta)$ as above. In other words, we assume x_i has a linear dependence on the stellar parameters.

Our aim is to derive the best estimator for the mean and variance of $x_{\rm True}$, i.e., $\hat{x}$ and $\mathrm{Var}(\hat{x})$. As all distributions are multivariate Gaussians, it is convenient to rewrite Equation (B1) in vector/matrix form as

$$x = x_{\rm True} I + M\psi, \tag{B2}$$

where x is the vector of all x_is; I is defined as the vector of N 1's; the vector ψ is a vector of all the random offsets with size $N + 4$,

$$\psi = \begin{pmatrix} \epsilon_1 \\ \vdots \\ \epsilon_N \\ \delta\theta_1 \\ \vdots \\ \delta\theta_4 \end{pmatrix}, \quad \psi \sim \mathcal{N}(0, \Sigma_\psi), \tag{B3}$$

where the covariance matrix Σ_ψ has e_i^2 on the diagonal augmented by the stellar parameter covariances, i.e.,

$$\Sigma_\psi = \begin{pmatrix} e_1^2 & 0 & \cdots & 0 & & \\ 0 & e_2^2 & & 0 & & 0 \\ \vdots & & \ddots & \vdots & & \\ 0 & \cdots & 0 & e_N^2 & & \\ & & 0 & & & \Sigma_\theta \end{pmatrix}, \tag{B4}$$

and the matrix M projects from $N + 4$ to N dimensions:

$$M = \begin{pmatrix} 1 & 0 & \cdots & 0 & G_{11} & G_{12} & G_{13} & G_{14} \\ 0 & 1 & \cdots & \vdots & \vdots & \vdots & \vdots & \vdots \\ \vdots & & \ddots & \vdots & \vdots & \vdots & \vdots & \vdots \\ 0 & \cdots & 0 & 1 & G_{N1} & G_{N2} & G_{N3} & G_{N4} \end{pmatrix}. \tag{B5}$$

Since M is a constant matrix and ψ is a multivariate Gaussian random vector, the distribution of $M\psi$ is

$$M\psi \sim \mathcal{N}(0, \widetilde{\Sigma}), \tag{B6}$$

$$\widetilde{\Sigma} = M\Sigma_\psi M^T; \tag{B7}$$

thus, our observed vector x is distributed $x \sim \mathcal{N}(x_{\rm True} I, \widetilde{\Sigma})$. The best estimator for the mean and variance of $x_{\rm True}$ is then

$$\hat{x} = \frac{I^T\widetilde{\Sigma}^{-1}x}{I^T\widetilde{\Sigma}^{-1}I}, \tag{B8}$$

$$\mathrm{Var}(\hat{x}) = \frac{1}{I^T\widetilde{\Sigma}^{-1}I}. \tag{B9}$$

Rather than construct and project down the augmented matrix, some tedious but straightforward algebra shows

$$\widetilde{\Sigma} = \mathrm{diag}(e_i^2) + \delta\rho\delta^T, \tag{B10}$$

where δ is the matrix of $\delta_{i,k} = G_{i,k}\sigma_k$ and ρ is the correlation matrix. Computationally, we use this form to calculate $\widetilde{\Sigma}$ rather than creating the augmented Σ_ψ and M matrices.

To get some intuition on this result, note that we can rewrite Equations (B8) and (B9) in terms of a weighted sum. If we define

$$\widetilde{w} = I^T\widetilde{\Sigma}^{-1} \tag{B11}$$

or $\widetilde{w}_i = \sum_j \widetilde{\Sigma}^{-1}_{ij}$, we see that

$$\hat{x} = \frac{\sum_i \widetilde{w}_i x_i}{\sum_i \widetilde{w}_i}, \tag{B12}$$

$$\mathrm{Var}(\hat{x}) = \frac{1}{\sum_i \widetilde{w}_i}, \tag{B13}$$

which looks like the usual inverse-variance weighted sum but using a different covariance matrix to determine the weights. Note that unlike an inverse variance, these weights can be negative, and they depend on the whole set of lines used to estimate the mean. The weights $\widetilde{w}_i$ are provided in Table 5.

The above calculations assume that each line provides an unbiased estimate of the total error. In reality, several additional systematic issues (e.g., atomic data uncertainties, 1D model atmospheres, and the LTE assumption) can cause substantial biases that are not averaged away. This is especially important when many lines are measured for a species (e.g., Fe I), as the systematic floor is well above the naive precision. To account for this, we use the observed line-to-line scatter to add a systematic floor to the per-line errors. We modify the model for ϵ_i to be $\epsilon_i \sim \mathcal{N}(0, e_i^2 + s_{\rm X}^2)$, where we have added a systematic uncertainty floor for each line of $s_{\rm X} \geqslant 0$. We can solve for $s_{\rm X}$ in terms of x_i, e_i, and the optimal estimator $\hat{x}$ by maximizing the log likelihood,

$$\begin{aligned} \log\mathcal{L} = &-0.5\sum_i \frac{(x_i - \hat{x})^2}{e_i^2 + s_{\rm X}^2} \\ &- 0.5\sum_i \log(e_i^2 + s_{\rm X}^2) + \text{constants}, \end{aligned} \tag{B14}$$

or, after taking the derivative with respect to $s_{\rm X}$ and setting to zero, solving

$$\sum_i \frac{(x_i - \hat{x})^2}{(e_i^2 + s_{\rm X}^2)^2} = \sum_i \frac{1}{e_i^2 + s_{\rm X}^2} \tag{B15}$$

for $s_{\rm X}$, which has to be done numerically. Since $\hat{x}$ depends on $s_{\rm X}$, we iterate between calculating $\hat{x}$ and numerically solving for $s_{\rm X}$ until reaching a precision <0.001 dex on $s_{\rm X}$. Then, in Equation (B10), we simply replace $\mathrm{diag}(e_i^2)$ with $\mathrm{diag}(e_i^2 + s_{\rm X}^2)$.

This model for the systematic errors is purely empirical, but in principle, a more physically motivated approach could be applied under this framework. As the simplest example, $s_{\rm X}$ can explicitly be set to include the $\log gf$ uncertainties reported in atomic data measurements (e.g., McWilliam et al. 2013). As a more complicated example, NLTE corrections could propagate

uncertainties in collisional or radiative rates to line-by-line corrections, which can modify both the mean and systematic uncertainty of a particular line.

Now that we have the optimal estimator for any species X, we consider the covariance between two species, X and Y. Let their optimal estimators be defined by $\hat{x} = U_{\rm X}^T x$, where $U_{{\rm X},i} = \widetilde{w}_i / \sum_j \widetilde{w}_j$; and similarly for Y. Also, let the gradient/difference matrices be $G_{\rm X}$ and $\delta_{\rm X} = G_{\rm X}\,{\rm diag}(\sigma_\theta)$, respectively, which are each $N \times 4$ matrices. Then,

$$\begin{aligned} {\rm Cov}(\hat{x}, \hat{y}) &= U_{\rm X}^T G_{\rm X} \Sigma_\theta G_{\rm Y}^T U_{\rm Y} \\ &= U_{\rm X}^T \delta_{\rm X} \rho \delta_{\rm Y}^T U_{\rm Y} \\ &\equiv \Delta_{\rm X} \rho \Delta_{\rm Y}^T, \end{aligned} \tag{B16}$$

where we have defined $\Delta_{\rm X} = U_{\rm X}^T \delta_{\rm X}$. Table 6 tabulates $\Delta_{\rm X}$ for all X, which we call Δ_T, Δ_g, Δ_v, and Δ_M in that table. These are morally equivalent to the table of stellar parameter uncertainty given in most high-resolution spectroscopy papers but include proper line weighting. Note that if calculating ${\rm Cov}(\hat{x}, \hat{x})$, make sure to use Equation (B9), which includes an extra statistical error term.

Finally, to wrap it all up, the error on $\log \epsilon\,({\rm X})$ (and thus also [X/H], since we assume the solar normalization is error-free) is simply $\sqrt{{\rm Var}(\hat{x})}$ from Equation (B9), which automatically includes all stellar parameter uncertainties and correlations. To find the error on the ratio of two species [X/Y], we use the fact that [X/Y] = [X/H] − [Y/H], so

$$\begin{aligned} {\rm Var}([{\rm X/Y}]) &= {\rm Var}(\hat{x} - \hat{y}) \\ &= {\rm Var}(\hat{x}) + {\rm Var}(\hat{y}) - 2{\rm Cov}(\hat{x}, \hat{y}) \end{aligned} \tag{B17}$$

and can be evaluated using Equations (B9) and (B16). Similarly, we can take the covariance between any set of element ratios, e.g., for elements A, B, C, D with estimators $\hat{a}$, $\hat{b}$, $\hat{c}$, $\hat{d}$,

$$\begin{aligned} {\rm Cov}([A/B], [C/D]) = {\rm Cov}(\hat{a}, \hat{c}) + {\rm Cov}(\hat{b}, \hat{d}) \\ - {\rm Cov}(\hat{a}, \hat{d}) - {\rm Cov}(\hat{b}, \hat{c}). \end{aligned} \tag{B18}$$

For pedagogical purposes, let us compare to two alternate estimators for $\hat{x}$ and ${\rm Var}(\hat{x})$ used in the literature. Most high-resolution studies do not calculate line-by-line uncertainties, instead taking a straight mean of all measured lines, i.e., $\hat{x} = \sum_i x_i / N = \sum_i x_i / \sum_i 1$. The error on the mean is usually found as the standard error, imposing a systematic floor (e.g., 0.1 dex) that is supposed to account for uncertainties in model atmospheres, atomic data, or other model uncertainties. This standard procedure weights every line equally, which is justifiable in the limit of carefully selected line measurements in very high-S/N data where systematic uncertainties (other than uncertain stellar parameters) dominate. However, in our red giants, where the blue flux is much lower than the red flux, lines are clearly measured in regions of different S/N. Furthermore, in low-S/N data, this procedure neglects the fact that the error on an individual line measurement is often much larger than the empirical deviation, especially if there are few lines for an element. The estimator provided here accounts for these issues at the considerable cost of having to compute uncertainties for individual lines.

To account for some of the issues described above, McWilliam et al. (1995) computed individual line uncertainties and combined them with a weighted mean. Each line was assigned an error $\sigma_i^2 = \sigma_{i,{\rm stat}}^2 + \sum_{k,l} \delta_{i,k} \delta_{i,l} \rho_{kl}$, i.e., the quadrature sum of random uncertainties and stellar parameter uncertainties including all cross terms. Then, using weights $w_i = 1/\sigma_i^2$, the mean was found with $\hat{x} = \sum_i (w_i x_i) / \sum_i w_i$ with an uncertainty ${\rm Var}(\hat{x}) = 1/\sum_i w_i$. However, this procedure ignores correlations between line abundances due to the fact that the same stellar parameters are used for all lines. In other words, it neglects the off-diagonal terms of $\widetilde{\Sigma}$, which usually results in moderately underestimated uncertainties. Ji et al. (2020) used the above procedure but added a systematic error that was estimated with the weighted standard error of the lines and added in quadrature to the statistical error. Compared to the analysis here, their overall error is a slight overestimate of the total uncertainty because it double-counts the random error.

Appendix C
Equivalent Width and Abundance Verification

To verify the equivalent width and corresponding abundance measurements, we performed an independent check of equivalent width and abundance measurements. Equivalent widths for two-thirds of our program stars were independently analyzed using `IRAF` and `MOOG` by T.T.H., including normalization, equivalent widths, model atmosphere interpolation, and abundance measurements. Equivalent widths were measured by fitting Gaussian profiles to the absorption lines in the continuum-normalized spectra using the `splot` task in `IRAF`.

Figure C1 shows the resulting equivalent width and abundance differences. The left column plots the difference between T.T.H.'s and A.P.J.'s equivalent widths. The right column plots the difference between T.T.H.'s and A.P.J.'s abundances. The red solid, dashed, and dotted lines show the median, 68% scatter, and 95% scatter in the difference, computed in bins of the x-axis. The top left panel shows the fractional equivalent width difference between the two measurements. The 1σ scatter is about 10%–15% at the lowest equivalent widths, decreasing to 5%–10% at higher equivalent widths. The top right panel shows that the typical 1σ scatter between individual line abundances is about 0.1 dex. There is no significant bias in the mean. The bottom two panels show the difference between equivalent width and abundance, normalized by the uncertainties in Table 5. As in the top panels, the median, 68% scatter, and 95% scatter in bins of the x-axis are plotted as red solid, dashed, and dotted lines, respectively. If the uncertainties are approximately Gaussian with no bias, then the dashed red lines should line up with ± 1 units on the y-axis, and the dotted red lines should line up at ± 2 units. The equivalent width uncertainties do indeed line up quite well with these values. The 68% scatter in abundance uncertainties also lines up well, but the tails are a little heavier, as the dashed red lines in the bottom right panel are around 2.5–3.0 instead of 2.0.

To verify the synthetic spectrum abundances, we selected seven stars covering the stellar parameter and S/N range of our stars: Chenab_12, Elqui_1, ATLAS_12, Indus_15, AliqaUma_7, Phoenix_2, and Phoenix_8. For these seven stars, abundances were independently derived using spectral synthesis via `MOOG` by T.T.H. The spectrum normalization, stellar parameters, and model atmospheres were independently determined.

The difference between the independent syntheses of individual features is shown in Figure C2. We show the differences normalized by two different abundance uncertainties of Table 5, the pure statistical error reported by SMHR e_i and the adjusted

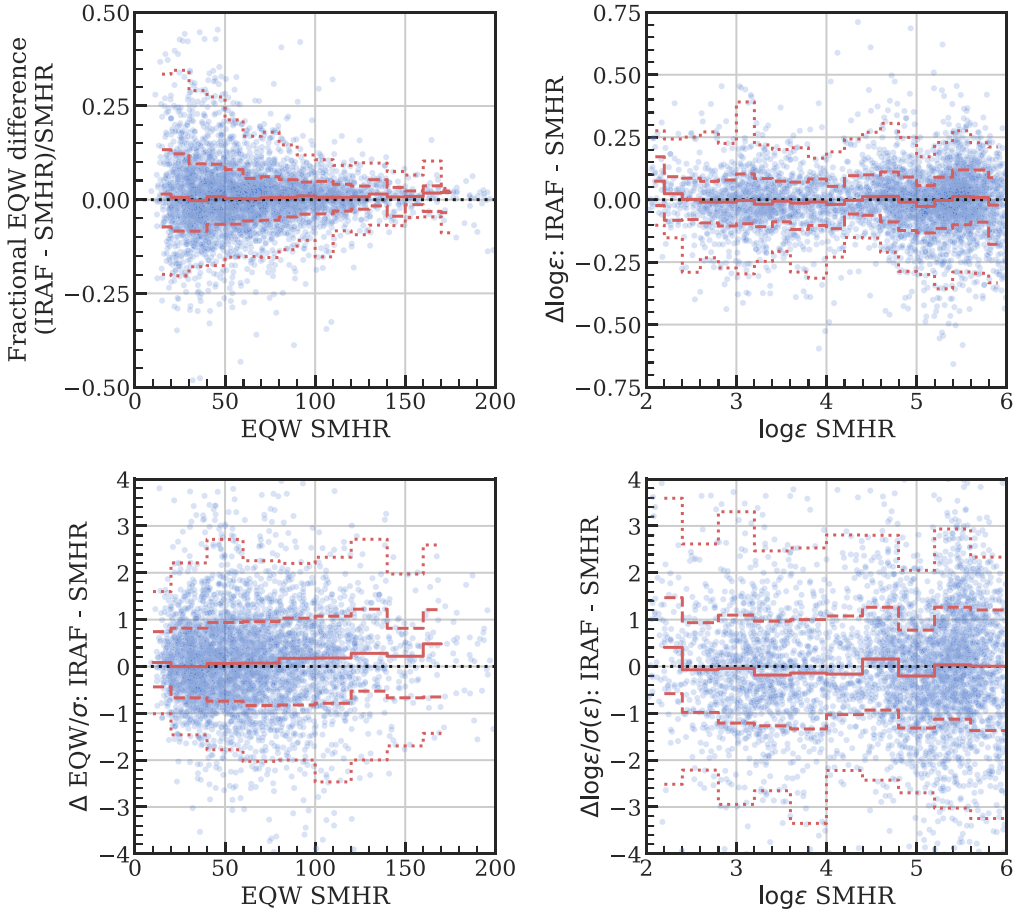

Figure C1. Verification of equivalent widths and abundances. Two of the authors (A.P.J. using `SMHR` and T.T.H. using `IRAF`) measured equivalent widths, interpolated model atmospheres, and measured abundances with independent methods but using the same stellar parameters, model atmosphere grid, and radiative transfer code. In all panels, blue points show differences between individual matched lines, while red dashed (dotted) lines show binned 68% (95%) scatter in bins of the x-axis. The top left panel shows the fractional difference in equivalent width of the measurements, showing the expected increase in scatter toward lower equivalent widths. The bottom left panel shows that after normalizing by the equivalent width uncertainties in Table 5, the differences are well described by Gaussian uncertainties. The top right panel shows that the typical scatter between equivalent width abundance measurements is about 0.1 dex, while the bottom right panel shows that the statistical abundance uncertainties are a good description of the differences.

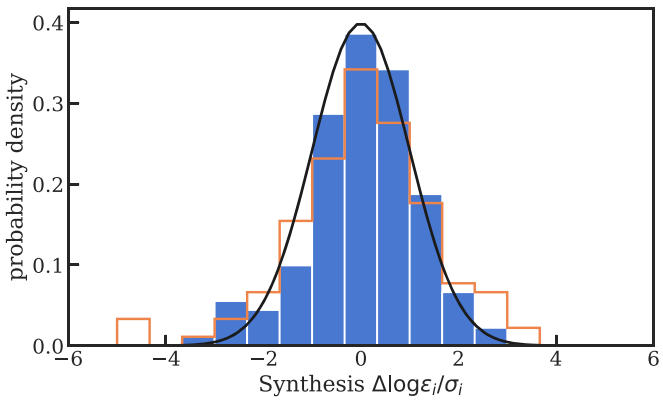

Figure C2. Difference between abundances in Table 5 and independent verification. The blue histogram is normalized by the total error σ_i in Table 5, while the slightly wider orange histogram is normalized by the pure statistical error e_i. The black line indicates the unit normal distribution.

systematic error σ_i, plotted as orange and blue histograms, respectively. The pure statistical uncertainties (orange) somewhat underestimate the observed dispersion. Line-by-line investigation shows the differences are primarily due to statistical errors that are too small for some Al, Sc, Mn, and Ba lines. For Al, the differences are mostly driven by systematics in continuum fitting, especially for the 3961 Å line that is in the wing of an H line. An extra 0.3 dex systematic error is added to account for this. The Sc and Mn lines have significant hyperfine splitting, and their abundance is more affected by the smoothing kernel applied to the synthetic spectrum. Reasonable changes in the smoothing kernel affect the abundances by up to 0.1 dex, so 0.1 dex systematic uncertainty is added to Sc and Mn. For Ba, we use strong lines with hyperfine splitting, and the resulting abundances are also sensitive to the smoothing kernel, so an extra 0.1 dex systematic uncertainty is added. Other lines with hyperfine structure are V, Co, La, and Eu. The existing statistical and systematic errors for these elements appear adequate, so we did not include any extra uncertainty for them. Including these systematic uncertainties, the normalized abundance differences (blue histogram in Figure C2) are close to normally distributed.

Appendix D
Abundance Correlations with Stellar Parameters

Figures D1–D3 show the abundance trends and correlations with respect to $T_{\rm eff}$, log g, and ν_t. The 1σ error ovals include correlations between the [X/Fe] abundance and a given

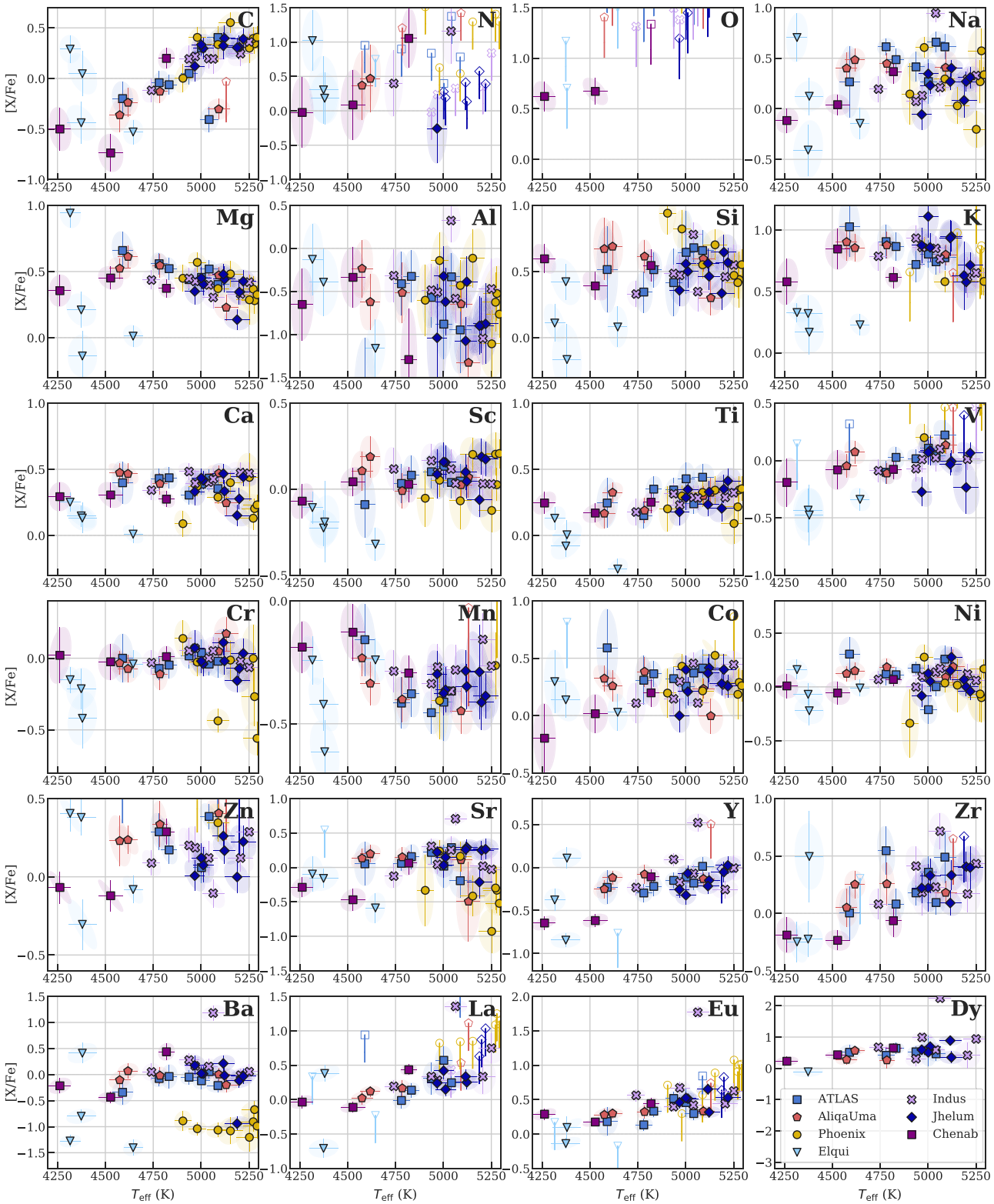

Figure D1. [X/Fe] vs. $T_{\rm eff}$.

stellar parameter. These are provided primarily as a way for users of the abundances to check for any systematic effects or estimate correlation effects due to stellar parameter uncertainties.

There are some important intrinsic correlations to mention. First, $T_{\rm eff}$, $\log g$, and ν_t are all highly correlated (Table 4, Figure 2). Thus, apparent correlations are not necessarily causal and should be checked against the typical orientation of the error ellipses. Second, warmer giants both tend to have weaker lines and are intrinsically less luminous. Third, due to intrinsic distance differences between the streams, stars in a given stream do not all occupy the same stellar parameters. The

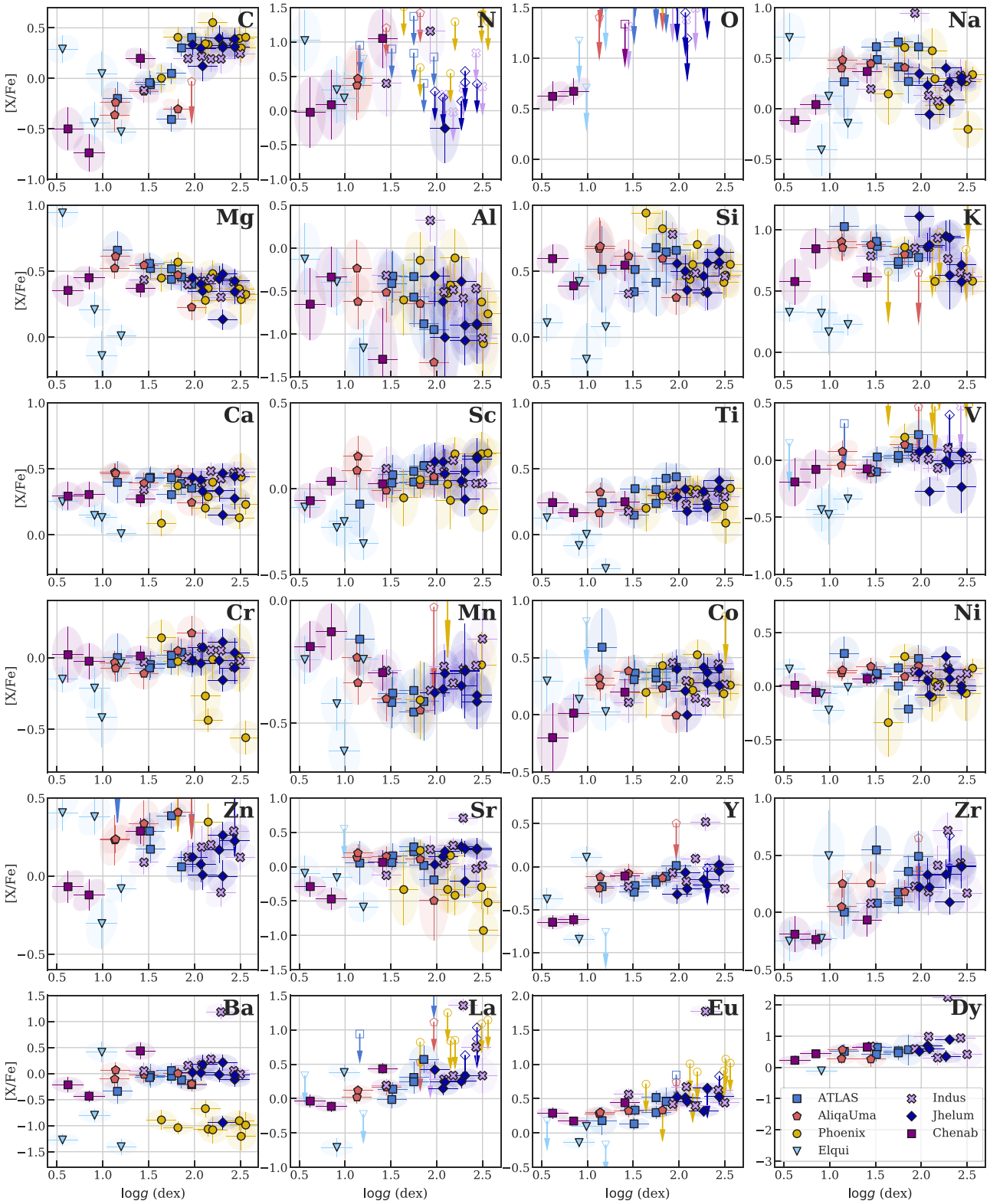

Figure D2. [X/Fe] vs. log g.

coolest stars in our sample (and thus lowest log g and highest ν_t stars) are in Chenab and Elqui; the warmest stars in our sample are in Phoenix, Jhelum, and Indus; and ATLAS and Aliqa Uma are in between. The differing intrinsic abundance trends in these streams thus clearly imprint on the correlations with stellar parameters.

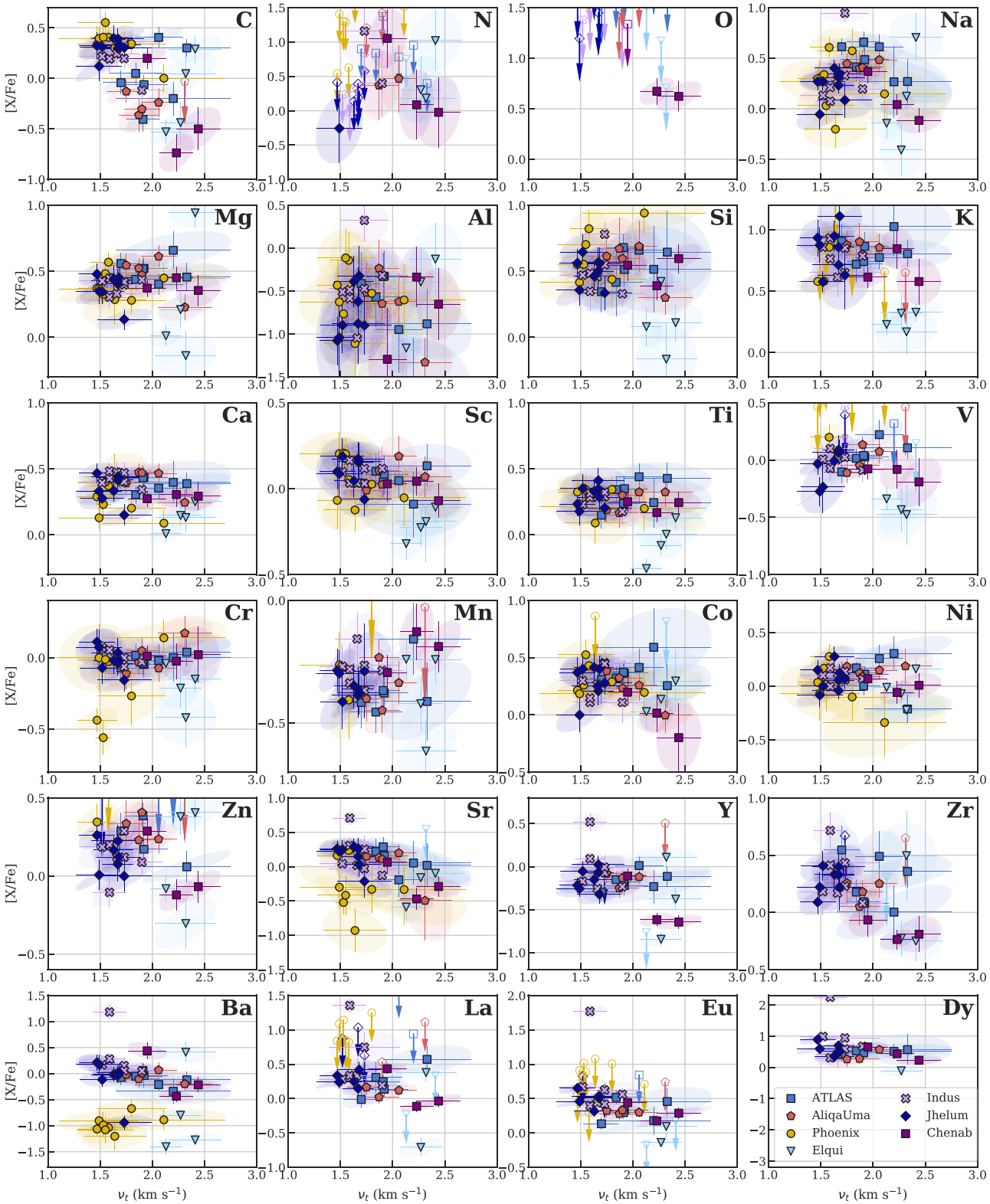

Figure D3. [X/Fe] vs. ν_t.

ORCID iDs

Alexander P. Ji https://orcid.org/0000-0002-4863-8842
Ting S. Li https://orcid.org/0000-0002-9110-6163
Terese T. Hansen https://orcid.org/0000-0001-6154-8983
Andrew R. Casey https://orcid.org/0000-0003-0174-0564
Sergey E. Koposov https://orcid.org/0000-0003-2644-135X
Andrew B. Pace https://orcid.org/0000-0002-6021-8760
Dougal Mackey https://orcid.org/0000-0002-6529-8093
Geraint F. Lewis https://orcid.org/0000-0003-3081-9319
Jeffrey D. Simpson https://orcid.org/0000-0002-8165-2507
Joss Bland-Hawthorn https://orcid.org/0000-0001-7516-4016
Lara R. Cullinane https://orcid.org/0000-0001-8536-0547
Gary. S. Da Costa https://orcid.org/0000-0001-7019-649X
Kohei Hattori https://orcid.org/0000-0001-6924-8862
Sarah L. Martell https://orcid.org/0000-0002-3430-4163
Kyler Kuehn https://orcid.org/0000-0003-0120-0808
Denis Erkal https://orcid.org/0000-0002-8448-5505
Nora Shipp https://orcid.org/0000-0003-2497-091X
Zhen Wan https://orcid.org/0000-0002-3105-3821
Daniel B. Zucker https://orcid.org/0000-0003-1124-8477

References

Abohalima, A., & Frebel, A. 2018, ApJS, 238, 36
Aoki, W., Arimoto, N., Sadakane, K., et al. 2009, A&A, 502, 569
Aoki, W., Honda, S., Sadakane, K., & Arimoto, N. 2007, PASJ, 59, L15
Asplund, M., Grevesse, N., Sauval, A. J., Allende Prieto, C., & Kiselman, D. 2004, A&A, 417, 751
Asplund, M., Grevesse, N., Sauval, A. J., & Scott, P. 2009, ARA&A, 47, 481
Astropy Collaboration, Robitaille, T. P., Tollerud, E. J., et al. 2013, A&A, 558, A33
Balbinot, E., Yanny, B., Li, T. S., et al. 2016, ApJ, 820, 58
Barklem, P. S., Christlieb, N., Beers, T. C., et al. 2005, A&A, 439, 129
Battaglia, G., North, P., Jablonka, P., et al. 2017, A&A, 608, A145
Belmonte, M. T., Pickering, J. C., Ruffoni, M. P., et al. 2017, ApJ, 848, 125
Belokurov, V., Erkal, D., Evans, N. W., Koposov, S. E., & Deason, A. J. 2018, MNRAS, 478, 611
Bergemann, M., & Cescutti, G. 2010, A&A, 522, A9
Bergemann, M., Gallagher, A. J., Eitner, P., et al. 2019, A&A, 631, A80
Bergemann, M., Lind, K., Collet, R., Magic, Z., & Asplund, M. 2012, MNRAS, 427, 27
Bergemann, M., Sesar, B., Cohen, J. G., et al. 2018, Natur, 555, 334
Bernstein, R., Shectman, S. A., Gunnels, S. M., Mochnacki, S., & Athey, A. E. 2003, Proc. SPIE, 4841, 1694
Biémont, É, Blagoev, K., Engström, L., et al. 2011, MNRAS, 414, 3350
Bonaca, A., Conroy, C., Price-Whelan, A. M., & Hogg, D. W. 2019, ApJL, 881, L37
Caffau, E., Ludwig, H. G., Steffen, M., et al. 2008, A&A, 488, 1031
Carlin, J. L., Sheffield, A. A., Cunha, K., & Smith, V. V. 2018, ApJL, 859, L10
Carpenter, B., Gelman, A., Hoffman, M. D., et al. 2017, JSS, 76, 1
Carretta, E., Bragaglia, A., Gratton, R., & Lucatello, S. 2009a, A&A, 505, 139
Carretta, E., Bragaglia, A., Gratton, R. G., et al. 2009b, A&A, 505, 117
Casagrande, L., & VandenBerg, D. A. 2014, MNRAS, 444, 392
Casey, A. R. 2014, PhD thesis, Australian National Univ.
Casey, A. R., Keller, S. C., Da Costa, G., Frebel, A., & Maunder, E. 2014, ApJ, 784, 19
Castelli, F., & Kurucz, R. L. 2003, in Proc. IAU Symp. 210, Modelling of Stellar Atmospheres, Poster Contributions, ed. N. Piskunov, W. W. Weiss, & D. F. Gray (San Fransisco, CA: ASP)
Chou, M.-Y., Cunha, K., Majewski, S. R., et al. 2010, ApJ, 708, 1290
Cohen, J. G., Christlieb, N., Thompson, I., et al. 2013, ApJ, 778, 56
Cohen, J. G., & Huang, W. 2009, ApJ, 701, 1053
Cohen, J. G., & Huang, W. 2010, ApJ, 719, 931
Cohen, J. G., & Kirby, E. N. 2012, ApJ, 760, 86
Cowan, J. J., Sneden, C., Roederer, I. U., et al. 2020, ApJ, 890, 119
de los Reyes, M. A. C., Kirby, E. N., Seitenzahl, I. R., & Shen, K. J. 2020, ApJ, 891, 85
Den Hartog, E. A., Lawler, J. E., Sneden, C., & Cowan, J. J. 2003, ApJS, 148, 543
Den Hartog, E. A., Lawler, J. E., Sneden, C., & Cowan, J. J. 2006, ApJS, 167, 292
Den Hartog, E. A., Lawler, J. E., Sneden, C., Cowan, J. J., & Brukhovesky, A. 2019, ApJS, 243, 33
Den Hartog, E. A., Lawler, J. E., Sobeck, J. S., Sneden, C., & Cowan, J. J. 2011, ApJS, 194, 35
Den Hartog, E. A., Ruffoni, M. P., Lawler, J. E., et al. 2014, ApJS, 215, 23
DES Collaboration, Abbott, T. M. C., Abdalla, F. B., et al. 2018, ApJS, 239, 18
Dotter, A., Chaboyer, B., Jevremović, D., et al. 2008, ApJS, 178, 89
Ezzeddine, R., Frebel, A., & Plez, B. 2017, ApJ, 847, 142
Foreman-Mackey, D., Hogg, D. W., Lang, D., & Goodman, J. 2013, PASP, 125, 306
Frebel, A., Casey, A. R., Jacobson, H. R., & Yu, Q. 2013a, ApJ, 769, 57
Frebel, A., Kirby, E. N., & Simon, J. D. 2010, Natur, 464, 72
Frebel, A., Lunnan, R., Casey, A. R., et al. 2013b, ApJ, 771, 39
Frebel, A., Norris, J. E., Gilmore, G., & Wyse, R. F. G. 2016, ApJ, 826, 110
Frebel, A., Simon, J. D., & Kirby, E. N. 2014, ApJ, 786, 74
Freeman, K., & Bland-Hawthorn, J. 2002, ARA&A, 40, 487
Fu, S. W., Simon, J. D., Shetrone, M., et al. 2018, ApJ, 866, 42
Fulbright, J. P. 2000, AJ, 120, 1841
Fulbright, J. P., Rich, R. M., & Castro, S. 2004, ApJ, 612, 447
Gaia Collaboration, Brown, A. G. A., Vallenari, A., et al. 2018, A&A, 616, A1
Gaia Collaboration, Prusti, T., de Bruijne, J. H. J., et al. 2016, A&A, 595, A1
Gallagher, A. J., Ludwig, H. G., Ryan, S. G., & Aoki, W. 2015, A&A, 579, A94
García Pérez, A. E., Allende Prieto, C., Holtzman, J. A., et al. 2016, AJ, 151, 144
Geisler, D., Smith, V. V., Wallerstein, G., Gonzalez, G., & Charbonnel, C. 2005, AJ, 129, 1428
Gilmore, G., Norris, J. E., Monaco, L., et al. 2013, ApJ, 763, 61
Gómez, F. A., Helmi, A., Cooper, A. P., et al. 2013, MNRAS, 436, 3602
Gratton, R., Bragaglia, A., Carretta, E., et al. 2019, A&ARv, 27, 8
Gratton, R., Sneden, C., & Carretta, E. 2004, ARA&A, 42, 385
Gratton, R. G., Carretta, E., & Bragaglia, A. 2012, A&ARv, 20, 50
Grillmair, C. J., & Carlberg, R. G. 2016, ApJL, 820, L27
Hannaford, P., Lowe, R. M., Grevesse, N., Biemont, E., & Whaling, W. 1982, ApJ, 261, 736
Hansen, C. J., El-Souri, M., Monaco, L., et al. 2018, ApJ, 855, 83
Hansen, T. T., Andersen, J., Nordström, B., et al. 2016, A&A, 588, A3
Hartwig, T., Yoshida, N., Magg, M., et al. 2018, MNRAS, 478, 1795
Hasselquist, S., Shetrone, M., Smith, V., et al. 2017, ApJ, 845, 162
Hayes, C. R., Majewski, S. R., Hasselquist, S., et al. 2020, ApJ, 889, 63
Helmi, A. 2020, ARA&A, in press
Helmi, A., Babusiaux, C., Koppelman, H. H., et al. 2018, Natur, 563, 85
Helmi, A., White, S. D. M., de Zeeuw, P. T., & Zhao, H. 1999, Natur, 402, 53
Hendricks, B., Boeche, C., Johnson, C. I., et al. 2016, A&A, 585, A86
Hill, V., Skúladóttir, Á, Tolstoy, E., et al. 2019, A&A, 626, A15
Hunter, J. D. 2007, CSE, 9, 90
Husser, T. O., Wende-von Berg, S., Dreizler, S., et al. 2013, A&A, 553, A6
Ibata, R. A., Malhan, K., & Martin, N. F. 2019, ApJ, 872, 152
Ishigaki, M. N., Aoki, W., Arimoto, N., & Okamoto, S. 2014, A&A, 562, A146
Jablonka, P., North, P., Mashonkina, L., et al. 2015, A&A, 583, A67
Jahandar, F., Venn, K. A., Shetrone, M. D., et al. 2017, MNRAS, 470, 4782
Ji, A. P., Frebel, A., Simon, J. D., & Chiti, A. 2016, ApJ, 830, 93
Ji, A. P., Li, T. S., Simon, J. D., et al. 2020, ApJ, 889, 27
Johnston, K. V., Bullock, J. S., Sharma, S., et al. 2008, ApJ, 689, 936
Jones, E., Oliphant, T., Peterson, P., et al. 2001, SciPy: Open Source Scientific Tools for Python, http://www.scipy.org/
Jönsson, H., Holtzman, J. A., Prieto, C. A., et al. 2020, AJ, 160, 120
Keller, S. C., Yong, D., & Da Costa, G. S. 2010, ApJ, 720, 940
Kelson, D. D. 2003, PASP, 115, 688
Kemp, A. J., Casey, A. R., Miles, M. T., et al. 2018, MNRAS, 480, 1384
Kirby, E. N., & Cohen, J. G. 2012, AJ, 144, 168
Kirby, E. N., Cohen, J. G., Smith, G. H., et al. 2011, ApJ, 727, 79
Kirby, E. N., Guhathakurta, P., Bolte, M., Sneden, C., & Geha, M. C. 2009, ApJ, 705, 328
Kirby, E. N., Xie, J. L., Guo, R., et al. 2019, ApJ, 881, 45
Koposov, S. E. 2019, RVSpecFit: Radial Velocity and Stellar Atmospheric Parameter Fitting, Astrophysics Source Code Library, ascl:1907.013
Koposov, S. E., Belokurov, V., Li, T. S., et al. 2019, MNRAS, 485, 4726
Koposov, S. E., Boubert, D., Li, T. S., et al. 2020, MNRAS, 491, 2465
Koposov, S. E., Gilmore, G., Walker, M. G., et al. 2011, ApJ, 736, 146
Koposov, S. E., Irwin, M., Belokurov, V., et al. 2014, MNRAS, 442, L85
Kos, J., Bland-Hawthorn, J., Freeman, K., et al. 2018, MNRAS, 473, 4612
Kramida, A., Ralchenko, Y., Reader, J. & NIST ASD Team 2019, NIST Atomic Spectra Database (version 5.7.1) (Gaithersburg, MD: NIST),
Kruijssen, J. M. D. 2019, MNRAS, 486, L20

Kruijssen, J. M. D., Pfeffer, J. L., Reina-Campos, M., Crain, R. A., & Bastian, N. 2019, MNRAS, 486, 3180
Krumholz, M. R., McKee, C. F., & Bland-Hawthorn, J. 2019, ARA&A, 57, 227
Kurucz, R., & Bell, B. 1995, Atomic Line Data, Kurucz CD-ROM No. 23 (Cambridge, MA: Smithsonian Astrophysical Observatory), 23
Larsen, S. S., Brodie, J. P., Grundahl, F., & Strader, J. 2014, ApJ, 797, 15
Lawler, J. E., Bonvallet, G., & Sneden, C. 2001a, ApJ, 556, 452
Lawler, J. E., & Dakin, J. T. 1989, JOSAB, 6, 1457
Lawler, J. E., Den Hartog, E. A., Sneden, C., & Cowan, J. J. 2006, ApJS, 162, 227
Lawler, J. E., Guzman, A., Wood, M. P., Sneden, C., & Cowan, J. J. 2013, ApJS, 205, 11
Lawler, J. E., Hala, Sneden, C., et al. 2019, ApJS, 241, 21
Lawler, J. E., Sneden, C., & Cowan, J. J. 2015, ApJS, 220, 13
Lawler, J. E., Sneden, C., Cowan, J. J., Ivans, I. I., & Den Hartog, E. A. 2009, ApJS, 182, 51
Lawler, J. E., Sneden, C., Nave, G., et al. 2017, ApJS, 228, 10
Lawler, J. E., Wickliffe, M. E., den Hartog, E. A., & Sneden, C. 2001b, ApJ, 563, 1075
Lawler, J. E., Wood, M. P., Den Hartog, E. A., et al. 2014, ApJS, 215, 20
Leaman, R. 2012, AJ, 144, 183
Lemasle, B., Hill, V., Tolstoy, E., et al. 2012, A&A, 538, A100
Letarte, B., Hill, V., Tolstoy, E., et al. 2010, A&A, 523, A17
Lewis, I. J., Cannon, R. D., Taylor, K., et al. 2002, MNRAS, 333, 279
Li, T. S., Koposov, S. E., Erkal, D., et al. 2020, arXiv:2006.10763
Li, T. S., Koposov, S. E., Zucker, D. B., et al. 2019, MNRAS, 490, 3508
Lind, K., Asplund, M., Barklem, P. S., & Belyaev, A. K. 2011, A&A, 528, A103
Ljung, G., Nilsson, H., Asplund, M., & Johansson, S. 2006, A&A, 456, 1181
Mackereth, J. T., & Bovy, J. 2020, MNRAS, 492, 3631
Majewski, S. R., Schiavon, R. P., Frinchaboy, P. M., et al. 2017, AJ, 154, 94
Majewski, S. R., Skrutskie, M. F., Weinberg, M. D., & Ostheimer, J. C. 2003, ApJ, 599, 1082
Marino, A. F., Villanova, S., Piotto, G., et al. 2008, A&A, 490, 625
Marshall, J. L., Hansen, T., Simon, J. D., et al. 2019, ApJ, 882, 177
Mashonkina, L. I., & Belyaev, A. K. 2019, AstL, 45, 341
Mashonkina, L. I., Sitnova, T. N., & Pakhomov, Y. V. 2016, AstL, 42, 606
Masseron, T., Plez, B., Van Eck, S., et al. 2014, A&A, 571, A47
Mateu, C., Read, J. I., & Kawata, D. 2018, MNRAS, 474, 4112
Matsuno, T., Aoki, W., & Suda, T. 2019, ApJL, 874, L35
Matteucci, F., & Brocato, E. 1990, ApJ, 365, 539
McKinney, W. 2010, in Python in Science Conf., ed. S. van der Walt & J. Millman (Austin, TX: SciPy), 56
McWilliam, A. 1998, AJ, 115, 1640
McWilliam, A., Piro, A. L., Badenes, C., & Bravo, E. 2018, ApJ, 857, 97
McWilliam, A., Preston, G. W., Sneden, C., & Searle, L. 1995, AJ, 109, 2757
McWilliam, A., Wallerstein, G., & Mottini, M. 2013, ApJ, 778, 149
Meléndez, J., & Barbuy, B. 2009, A&A, 497, 611
Monaco, L., Bellazzini, M., Bonifacio, P., et al. 2007, A&A, 464, 201
Mucciarelli, A., Bellazzini, M., Ibata, R., et al. 2012, MNRAS, 426, 2889
Muñoz, R. R., Côté, P., Santana, F. A., et al. 2018, ApJ, 860, 66
Myeong, G. C., Vasiliev, E., Iorio, G., Evans, N. W., & Belokurov, V. 2019, MNRAS, 488, 1235
Naidu, R. P., Conroy, C., Bonaca, A., et al. 2020, arXiv:2006.08625
Nidever, D. L., Holtzman, J. A., Allende Prieto, C., et al. 2015, AJ, 150, 173
Nordlander, T., & Lind, K. 2017, A&A, 607, A75
Norris, J. E., Wyse, R. F. G., Gilmore, G., et al. 2010a, ApJ, 723, 1632
Norris, J. E., Yong, D., Gilmore, G., & Wyse, R. F. G. 2010b, ApJ, 711, 350
Norris, J. E., Yong, D., Venn, K. A., et al. 2017, ApJS, 230, 28
O'Brian, T. R., Wickliffe, M. E., Lawler, J. E., Whaling, W., & Brault, J. W. 1991, JOSAB, 8, 1185
Placco, V. M., Frebel, A., Beers, T. C., & Stancliffe, R. J. 2014, ApJ, 797, 21
Price-Whelan, A. M., Sipőcz, B. M., Günther, H. M., et al. 2018, AJ, 156, 123
Pritzl, B. J., Venn, K. A., & Irwin, M. 2005, AJ, 130, 2140
Reggiani, H., Amarsi, A. M., Lind, K., et al. 2019, A&A, 627, A177
Rocha, M., Peter, A. H. G., & Bullock, J. 2012, MNRAS, 425, 231
Roederer, I. U., & Gnedin, O. Y. 2019, ApJ, 883, 84
Roederer, I. U., & Lawler, J. E. 2012, ApJ, 750, 76
Roederer, I. U., Mateo, M., Bailey, J. I., III, et al. 2016, AJ, 151, 82
Roederer, I. U., Preston, G. W., Thompson, I. B., et al. 2014, AJ, 147, 136
Roederer, I. U., Sneden, C., Thompson, I. B., Preston, G. W., & Shectman, S. A. 2010, ApJ, 711, 573
Roediger, J. C., Courteau, S., Graves, G., & Schiavon, R. P. 2014, ApJS, 210, 10
Ruffoni, M. P., Den Hartog, E. A., Lawler, J. E., et al. 2014, MNRAS, 441, 3127
Ryabchikova, T., Piskunov, N., Kurucz, R. L., et al. 2015, PhyS, 90, 054005
Sakari, C. M., Placco, V. M., Hansen, T., et al. 2018, ApJL, 854, L20
Schlegel, D. J., Finkbeiner, D. P., & Davis, M. 1998, ApJ, 500, 525
Sharp, R., Saunders, W., Smith, G., et al. 2006, Proc. SPIE, 6269, 62690G
Shetrone, M., Bizyaev, D., Lawler, J. E., et al. 2015, ApJS, 221, 24
Shetrone, M., Venn, K. A., Tolstoy, E., et al. 2003, AJ, 125, 684
Shetrone, M. D., Côté, P., & Sargent, W. L. W. 2001, ApJ, 548, 592
Shipp, N., Drlica-Wagner, A., Balbinot, E., et al. 2018, ApJ, 862, 114
Shipp, N., Li, T. S., Pace, A. B., et al. 2019, ApJ, 885, 3
Simmerer, J., Sneden, C., Cowan, J. J., et al. 2004, ApJ, 617, 1091
Simon, J. D. 2019, ARA&A, 57, 375
Simon, J. D., Jacobson, H. R., Frebel, A., et al. 2015, ApJ, 802, 93
Simpson, J. D., Martell, S. L., Da Costa, G., et al. 2020, MNRAS, 491, 3374
Sneden, C., Cowan, J. J., & Gallino, R. 2008, ARA&A, 46, 241
Sneden, C., Cowan, J. J., Kobayashi, C., et al. 2016, ApJ, 817, 53
Sneden, C., Lawler, J. E., Cowan, J. J., Ivans, I. I., & Den Hartog, E. A. 2009, ApJS, 182, 80
Sneden, C., Lucatello, S., Ram, R. S., Brooke, J. S. A., & Bernath, P. 2014, ApJS, 214, 26
Sneden, C. A. 1973, PhD thesis, The Univ. of Texas at Austin
Sobeck, J. S., Kraft, R. P., Sneden, C., et al. 2011, AJ, 141, 175
Sobeck, J. S., Lawler, J. E., & Sneden, C. 2007, ApJ, 667, 1267
Stan Development Team 2018, PyStan: The Python Interface to Stan, Version 2.17.1.0, http://mc-stan.org
Stoughton, C., Lupton, R. H., Bernardi, M., et al. 2002, AJ, 123, 485
Tafelmeyer, M., Jablonka, P., Hill, V., et al. 2010, A&A, 524, A58
Tinsley, B. M. 1980, FCPh, 5, 287
Tolstoy, E., Hill, V., & Tosi, M. 2009, ARA&A, 47, 371
Skúladóttir, Á, Tolstoy, E., Salvadori, S., et al. 2015, A&A, 574, A129
Tsujimoto, T., Ishigaki, M. N., Shigeyama, T., & Aoki, W. 2015, PASJ, 67, L3
Tsujimoto, T., Matsuno, T., Aoki, W., Ishigaki, M. N., & Shigeyama, T. 2017, ApJL, 850, L12
Ural, U., Cescutti, G., Koch, A., et al. 2015, MNRAS, 449, 761
van der Walt, S., Colbert, S. C., & Varoquaux, G. 2011, CSE, 13, 22
Venn, K. A., Irwin, M., Shetrone, M. D., et al. 2004, AJ, 128, 1177
Venn, K. A., Shetrone, M. D., Irwin, M. J., et al. 2012, ApJ, 751, 102
Venn, K. A., Starkenburg, E., Malo, L., Martin, N., & Laevens, B. P. M. 2017, MNRAS, 466, 3741
Wan, Z., Lewis, G. F., Li, T. S., et al. 2020, Natur, 583, 768
Waskom, M., Botvinnik, O., O'Kane, D., et al. 2016, seaborn: v0.7.0 (2016 January), Zenodo, doi:10.5281/zenodo.45133
Wenger, M., Ochsenbein, F., Egret, D., et al. 2000, A&AS, 143, 9
Willman, B., & Strader, J. 2012, AJ, 144, 76
Wilson, J. C., Hearty, F. R., Skrutskie, M. F., et al. 2019, PASP, 131, 055001
Wood, M. P., Lawler, J. E., Den Hartog, E. A., Sneden, C., & Cowan, J. J. 2014a, ApJS, 214, 18
Wood, M. P., Lawler, J. E., Sneden, C., & Cowan, J. J. 2013, ApJS, 208, 27
Wood, M. P., Lawler, J. E., Sneden, C., & Cowan, J. J. 2014b, ApJS, 211, 20
Yong, D., Meléndez, J., Grundahl, F., et al. 2013, MNRAS, 434, 3542
York, D. G., Adelman, J., Anderson, J. E. J., et al. 2000, AJ, 120, 1579
Yuan, Z., Myeong, G. C., Beers, T. C., et al. 2020, ApJ, 891, 39
Zasowski, G., Cohen, R. E., Chojnowski, S. D., et al. 2017, AJ, 154, 198